Modeling of Chemical Mechanical Polishing for Shallow Trench Isolation

by
Terence Gan

Submitted to the
Department of Electrical Engineering and Computer Science
in Partial Fulfillment of the Requirements for the Degrees of

Bachelor of Science in Electrical Science and Engineering
and Master of Engineering in Electrical Engineering and Computer Science

at the

MASSACHUSETTS INSTITUTE OF TECHNOLOGY

May 8, 2000
[June 2000]

© Copyright 2000 Massachusetts Institute of Technology. All rights reserved.

Author ______________________________
Department of Electrical Engineering and Computer Science
May 8, 2000

Certified by ______________________________
Duane S. Boning
Associate Professor of EECS, Thesis Supervisor

Accepted by ______________________________
Arthur C. Smith
Chairman, Department Committee on Graduate Theses

ENG

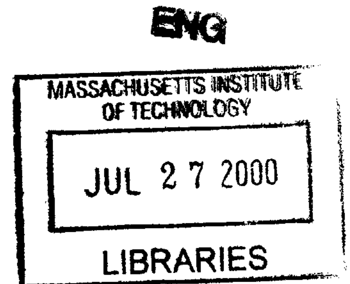
MASSACHUSETTS INSTITUTE OF TECHNOLOGY
JUL 27 2000
LIBRARIES

Modeling of Chemical Mechanical Polishing for Shallow Trench Isolation

by
Terence Gan

Submitted to the
Department of Electrical Engineering and Computer Science

May 8, 2000

In Partial Fulfillment of the Requirements for the Degrees of
Bachelor of Science in Electrical Science and Engineering
and Master of Engineering in Electrical Engineering and Computer Science

ABSTRACT

Shallow trench isolation (STI) has emerged as the primary technique for device isolation for advanced ULSI CMOS technologies. STI is desirable because it has near zero field encroachment, good latch-up immunity, good planarity, and low junction capacitance. STI is also highly scalable, and trench-fill capabilities are the only major challenge to scaling. However, STI requires a planarization procedure, such as chemical mechanical polishing (CMP). CMP not only increases the process complexity, but also suffers from die-level layout pattern dependencies which makes it difficult to completely remove the oxide above the large nitride areas. This problem can be solved using reverse tone etch back, which removes the oxide over large nitride areas prior to CMP. A model for reverse tone etch back is needed to obtain knowledge and insight that will reduce development cycle times and cost. This thesis presents a comprehensive model for reverse tone etch back STI CMP that incorporates density averaging effects for small pre-CMP step height. STI CMP characterization experiments are performed and the results are used to validate the proposed model. Using the model, the effects of pre-CMP step height, pattern density, polish time, pad hardness, and slurry selectivity on dishing and erosion are predicted.

Thesis Supervisor: Duane S. Boning
Title: Associate Professor of EECS

Acknowledgements

My first thanks go out to my academic and thesis advisor Professor Duane Boning, to whom I am extremely honored and grateful for inviting me to join his research group in Fall of 1998. Even though my progress in research was slow and results were scant, he never ceased to inspire me with new research ideas and provide me with numerous opportunities to expand my knowledge of CMP. This work is the culmination of his trust in me. I hope that I have made him proud.

Most of my experimental work was done at the Taiwan Semiconductor Manufacturing Company (TSMC) in Hsin-Chu, Taiwan, as part of the Microsystems Industrial Group (MIG) program at the MIT Microsystems Technology Laboratories (MTL). I wish to thank Vicky Diadiuk, Assistant Director of Operations at MTL, as well as the staff at MTL, TSMC, the Taipei Economic and Cultural Office in Boston, and the MIT International Students Office, for working so hard to make my Summer internship at TSMC possible.

Many thanks go out to all my colleagues and friends at TSMC who were such warm and hospitable hosts. First of all, I wish to thank Dr. Shang-Yi Chiang, Vice President, R&D, TSMC, for giving me this opportunity to work in TSMC; my mentors Douglas Yu and Simon Jang, who made sure that I had all the help I needed; C. L. Chang, who was like a big brother and always there to help me whenever I encountered problems; C. H. Lin and H. T. Lin for teaching me how to use L-Edit to create the STI CMP characterization masks; T. I. Bao for lending me his bicycle, on which I commuted to work almost everyday; F. Y. Wang for her friendship; H. W. Lin and C. Y. Lin for teaching me how to operate the SEM; J. Y. Cheng, Y. H. Chen, C. Y. Fu, T. Shih, L. Y. Su, J. M. Peng and others in the TFD R&D group for their friendship. Last but not least, I wish to thank the engineers, support staff and operators in Fab 3 and 4 who helped me in one way or another.

I will also like to thank Mr. Tan Su Bin and family who lived next door to me in Taiwan. They were like a host family to me, making sure I was well settled in and never hungry or lonely.

Here at MIT, I wish to thank the technical staff at MTL: Kurt Broadrick, Barry Farnsworth, Paul Tierney, and Joe Walsh just to name a few; my colleagues in the Metrology Group: Brian Lee for the interesting discussions about CMP and help with SiCat, Tamba Tugbawa for modeling insight and from whose work I have greatly benefited, Tae Park for his invaluable help with Cadence, Vikas Mehrotra, Shiou-Lin Sam, Radhika Dutt, David White, Angie Nishimoto, Charles Oiji, and Dennis Ouma; my office mates Aaron Gower and Kuang Han Chen for their help with Matlab.

Special thanks go to Dawen Choy, Jessica Tan, Philip Tan, and Tracey Ho, for all the sumptuous dinners we prepared together, and I could always rely on them for some entertainment after a hard day's work. I also wish to thank all my friends in the Singapore Students Society, the Malaysian Students Association, and all my other friends in MIT for making my four years here so memorable. Special mention goes to my friends in the MIT Figure Skating Club, with whom I spent almost all my weekends: my coach Louise Silver, my skating partner Angela Yu, Joyance Meechai, Bev Thurber, Bill Rowe, Barb

Cutler, Derek Breuning, Esther Horwich, Trish Fleming, Sally DeFazio, John Porter, and others.

My deepest thanks go to my family in Singapore: my dad, mom, and brother, whose moral support and encouragement have given me the confidence to come this far. I also wish to thank my grandma, I pray you live a long and healthy life; auntie Annie, now I hope I will be able to go travelling with you as promised; auntie Nancy and uncle Peter, thanks for your encouragement; and my darling cousins Alicia, Arena, and Amelia, I hope to be a good role model for you. Finally, there is a special place in my heart reserved for my girlfriend, Meizhen. I do not know how to thank you enough for helping me stay focused on my work, and loving me from halfway around the Earth.

Last but not least, I thank my sponsor, the Singapore Economic Development Board. With your financial support, I was able to come to MIT and need not worry about having enough money to pay my tuition.

To all my family and friends, I dedicate this work to you.

This work was supported in part by a DARPA subcontract with PDF Solutions, Inc.

Table of Contents

Chapter 1 Introduction **10**

1.1 Motivation for Device Isolation 11

1.2 Device Isolation Techniques 13

1.2.1 Local Oxidation of Silicon 13

1.2.2 Shallow Trench Isolation 16

1.3 Thesis Goals 18

1.4 Thesis Organization 19

Chapter 2 Chemical Mechanical Polishing for STI **20**

2.1 Overview of Dielectric CMP 20

2.2 Shallow Trench Isolation CMP 23

2.3 Reverse Tone Etch Back STI 25

Chapter 3 Modeling of Reverse Tone Etch Back STI CMP **27**

3.1 Previous Work 28

3.1.1 Density Dependent CMP Model 28

3.1.2 Removal Rate vs. Step Height CMP Model 29

3.2 Model Formulation 30

3.3 Mathematical Relations 34

3.3.1 Steady State Dishing 35

3.3.2 Step Height 35

3.3.3 Nitride Erosion 37

3.4 Experimental Details 38

3.4.1 The STI CMP Characterization Mask 38

3.4.2 Process Conditions 42

3.5 Parameter Extraction Methodology 43

3.6 Results and Discussion 45

3.6.1 Oxide-Nitride Selectivity 51

3.6.2 Polish Time Constant, τ 51
3.6.3 Steady State Dishing, d_{ss} 52
3.6.4 Pad Deformation Limit, d_{max} 53
3.7 Additional Modeling Results 55
3.7.1 Pattern Density 55
3.7.2 Initial Step Height 58
3.7.3 Oxide to Nitride Selectivity 60

Chapter 4 Combined Planarization Length Parameter Extraction Methodology 62

4.1 Density Averaging using Planarization Length 63
4.2 Updated Parameter Extraction Methodology 66
4.3 Results and Discussion 68

Chapter 5 Conclusion and Future Work 71

5.1 STI CMP Modeling 71
5.2 Applications of the Methodology 72
5.3 Future Work 73
5.3.1 Validation on Non-Standard Structures 73
5.3.2 Process Variations 73
5.3.3 Steady-State Dishing (d_{ss}) and Pad Deformation Limit (d_{max}) 74
5.3.4 K_{ox} and K_{nit} 74

Bibliography 75

Appendix 78

A-1 Planarization Length Optimization for Process A 78
A-2 Density and Parameter Extraction for Process A 79
A-3 Cost Function for Process A 80
B-1 Planarization Length Optimization for Process B 83
B-2 Density and Parameter Extraction for Process B 84
B-3 Cost Function for Process B 85
C-1 Planarization Length Optimization for Process C 88

C-2 Density and Parameter Extraction for Process C 89
C-3 Cost Function for Process C 90
D Effective Density Extractor 93
E Density Map Generator 94
F Density Averaging 95
G Matrix Shift 97

List of Figures

1.1 Parasitics in NMOS transistor 12
1.2 Parasitics in CMOS transistor 12
1.3 Simplified pnpn thyristor model for a CMOS inverter 13
1.4 LOCOS process summary 15
1.5 STI process summary 17
2.1 Examples of CMP tools 21
2.2 Possible oxide CMP mechanism 22
2.3 Effect of pad rigidity on planarity 23
2.4 Problems with conventional STI CMP 24
2.5 Modified process flow for reverse tone etch back STI CMP 26
3.1 Cross-section of a reverse tone etch back STI structure 31
3.2 Removal rate vs. step height model for reverse tone etch back STI CMP 32
3.3 Close-up of STI CMP characterization masks 39
3.4 Schematic of STI CMP characterization mask 41
3.5 Actual and predicted step height for process A 48
3.6 Actual and predicted step height for process B 49
3.7 Actual and predicted step height for process C 50
3.8 Dependence of τ, d_{ss}, and d_{max} on density 54
3.9 Time evolution of step height and nitride erosion on pattern density 57
3.10 Effect of pre-CMP step height on post-CMP step height 59
3.11 Effect of high selectivity slurry on step height and nitride erosion 61
4.1 Physical meaning of planarization length 63
4.2 Density averaging 64
4.3 Effective density distribution for different planarization lengths 65
4.4 Flow chart of updated parameter extraction methodology 67
4.5 Effective density vs. pattern density 70

List of Tables

3.1 Summary of CMP conditions 43

3.2 Summary of results from parameter extraction 46

3.3 RMS errors for step height and nitride erosion 47

4.1 RMS errors using the updated parameter extraction methodology 69

5.1 Expected and extracted values for K_{ox}, K_{nit}, and selectivity 74

Chapter 1
Introduction

Shallow trench isolation (STI) has emerged as the primary technique for device isolation for advanced ULSI CMOS technologies [1]-[3]. DRAM and microprocessor products are currently the technology drivers for the whole semiconductor industry. The International Technology Roadmap for Semiconductors predicts that DRAM half-pitch and microprocessor gate length will reach 100 nm and 65 nm respectively in 2005, from 180 nm and 140 nm today. In the same period, the transistor density for logic (high-volume microprocessor) at introduction is expected to increase from 6.6 million transistors per cm^2 per chip to 44 million transistors per cm^2 [4]. This is driven by the need to maintain the historical trend of reducing cost per function by 25-30% per year while accommodating 59% more bits/capacitors/transistors per year in accordance with Moore's Law [4]. To satisfy the high density requirements of modern integrated circuits, device isolation is needed. STI is the preferred technique for deep sub-micron applications.

This chapter summarizes the main techniques and issues in device isolation. Section 1.1 discusses the reasons for device isolation. Section 1.2 presents an overview of some isolation techniques and their limitations. Section 1.3 defines the scope of this thesis, and finally, Section 1.4 details the thesis organization.

1.1 Motivation for Device Isolation

An important part of integrated circuit design is directed towards keeping the basic device characteristics as close to ideal as possible. This means reducing parasitic conduction paths and series resistances, maintaining threshold voltage control, and minimizing the leakage current of the device. However, in order to increase the gross number of chips available on a wafer, a combination of smaller feature sizes (scaling and shrink) and product redesign (compaction) is used. Compaction reduces the separation between adjacent devices, which increases the chance of device failure via parasitic conduction paths and latch up. Device isolation can prevent parasitic conduction and latch up and this is discussed below.

Parasitic conduction occurs between adjacent NMOS transistors due to the formation of a parasitic transistor as shown in Figure 1.1. The parasitic NMOS transistor consists of a polysilicon gate with the field oxide acting as a gate oxide and the channel-stop region as the channel. Compaction shortens the channel length of the parasitic transistor, and this increases the leakage current. The active transistors can be isolated by making the field oxide as thick as possible and the channel-stop as heavily doped as possible [5].

Similarly, a parasitic n-channel transistor can form between the n+ source and the adjacent n-tub, and a parasitic p-channel transistor exists between the p+ source and the adjacent p-tub in CMOS circuits as shown in Figure 1.2.

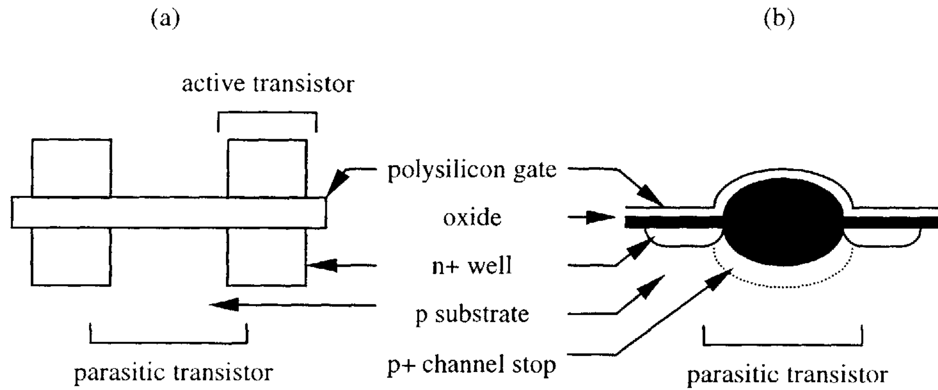

Figure 1.1 Parasitic transistor in NMOS: (a) top view of adjacent NMOS transistors sharing a common gate, (b) cross-section view showing the npn parasitic transistor.

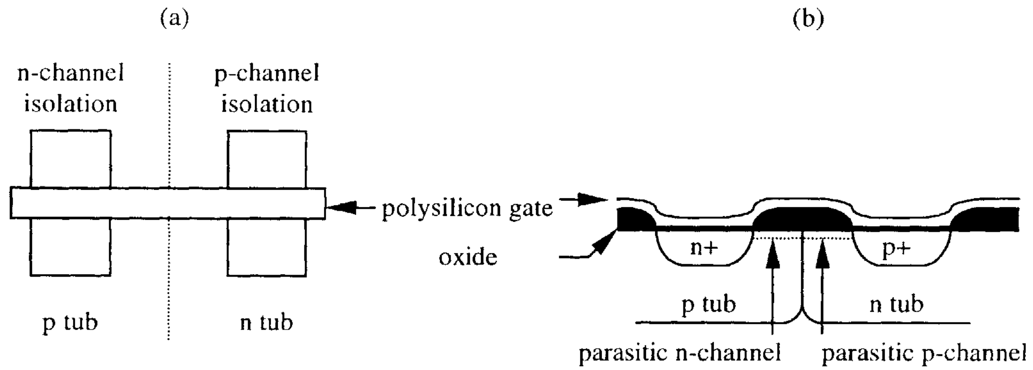

Figure 1.2 Parasitics in CMOS transistor: (a) top view of adjacent n- and p-channel transistors sharing a common polysilicon gate, (b) parasitic n- and p-channels.

Latch up occurs in CMOS circuits when the source/drain regions are in close proximity to an adjacent tub. The source/drain regions and the tubs form parasitic bipolar transistors that make up a thyristor (pnpn) device as shown in Figure 1.3. The thyristor can be biased such that the collector current of the pnp device supplies a base current to the npn device in a positive feedback arrangement. This produces a large sustained current between the positive and negative terminals of the thyristor and may cause the CMOS circuit to cease functioning or even self-destruct [5]. The parasitic bipolar

transistors can be decoupled in several ways, including physically separating the transistors via trench isolation.

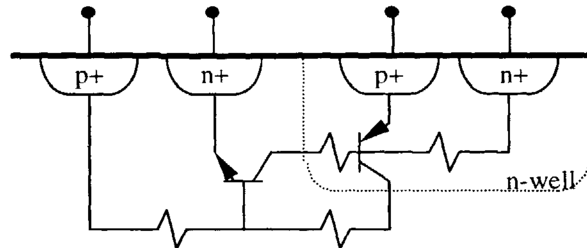

Figure 1.3 Simplified pnpn thyristor model for a CMOS inverter.

1.2 Device Isolation Techniques

In integrated circuits, devices such as transistors are fabricated on a common piece of silicon. Without proper device isolation, these devices will interact with one another in undesirable ways. The need for a scalable CMOS isolation technology is critical in order to advance into the 0.25 μm 256Mbit DRAM generation and beyond. The geometric characteristics of ideally scalable isolation technology are (1) an abrupt transition from active MOSFET regions to isolation regions, (2) independence of isolation width and depth, and (3) planarity [3]. This section describes the key features of two of the most well-known device isolation techniques for ULSI applications: LOCOS and shallow trench isolation (STI).

1.2.1 Local Oxidation of Silicon

Local oxidation of silicon (LOCOS) has been the most dominant isolation process used in IC technologies for the last two decades, mainly due to simplicity and low cost.

However, as semiconductor devices scale down to sub-0.5 μm geometries, the practicality of conventional LOCOS is questioned. The main drawbacks of conventional LOCOS are bird's beak formation, field-implant encroachment, field oxide thinning at narrow dimensions, and topography [3,6].

LOCOS utilizes the property that oxygen diffuses through silicon nitride (Si_3N_4) very slowly, so a thick layer of oxide (SiO_2) can be preferentially grown to laterally isolate devices. Figure 1.4 shows the major process steps. A thin layer of pad oxide is first thermally grown on a clean silicon surface. Next, a thick layer of chemical vapor deposition (CVD) silicon nitride, which functions as the oxidation mask, is deposited. The nitride/oxide composite layer is then patterned and etched, followed by a field implant to form the channel-stop. The wafer is then oxidized. The nitride acts as a barrier to the diffusion of oxygen and prevents oxidation of the silicon below the nitride. Since oxidation consumes 44% as much silicon as it grows, the resultant oxide is partially recessed. Lateral diffusion of oxygen under the edges of the nitride causes some silicon under the nitride to be oxidized. The process leaves a characteristic structure called a bird's beak because it is shaped like the beak of a bird. Finally, the masking nitride layer is stripped and the pad oxide is etched [7,8].

The existence of the bird's beak reduces the amount of current that a transistor can drive. As shown in Figure 1.3, the bird's beak encroaches laterally into the silicon under the nitride. This reduces the active width of the device, which reduces its drive current.

In order to grow the thick layer of oxide needed for device isolation, high temperatures and long oxidation times are needed. The high thermal budget causes the

dopants in the channel-stop to diffuse into the edges of the active region. The resultant transistor behaves as if it is a narrower device, and this further reduces its drive current.

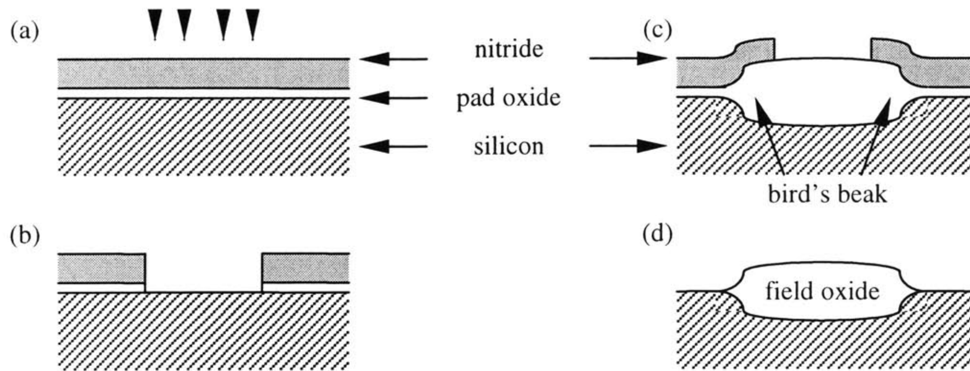

Figure 1.4 LOCOS process summary: (a) pad oxide and nitride deposition, (b) pattern and etch, (c) oxide growth, (d) nitride and pad oxide stripping.

LOCOS also suffers from field oxide thinning which degrades planarity and results in shallow isolation. The thickness of the field oxide varies strongly with isolation space. In particular, field oxide thinning increases with decreasing isolation space [3,6]. Hence, it creates topography between wide isolation regions and narrow isolation regions. Furthermore, LOCOS-based isolations are shallow because more than half of the as-grown oxide thickness is above the silicon surface. Field oxide thinning causes the junction to be even shallower, and the junction may not be sufficiently deep to keep isolation implants from impacting junction and device characteristics [3].

As mentioned earlier, more than half of the as-grown oxide thickness is above the silicon surface. Hence, LOCOS creates significant topography. Non-planarity results in poor linewidth control during subsequent lithographic and etching processing [3].

Traditional LOCOS has serious has many serious limitations in the sub-micrometer regime that limit the minimum active area pitch that can be achieved. Several

advanced LOCOS processes have been proposed, that reduce the minimum active area pitch to 0.9 μm and 0.6 μm for 64 Mbit and 256 Mbit DRAM respectively. However, for pitch values below 0.6 μm, the field oxide thinning effect inherent in all LOCOS-based technologies, results in unacceptable parasitic field devices characteristics [10].

1.2.2 Shallow Trench Isolation

Shallow trench isolation (STI) is the preferred isolation scheme for applications based on ULSI CMOS technologies with active area pitches in the sub-0.5 μm regime. STI is preferred over LOCOS because it has near zero field encroachment, good latch-up immunity, better planarity, and low junction capacitance [1,2,3]. STI is also highly scalable, the trench-fill capabilities being the only major challenge to scaling [3]. However, STI requires a planarization procedure that increases the process complexity.

STI is fabricated using a damascene process. Figure 1.5 shows the major STI process steps. A thin layer of pad oxide is first grown on a clean silicon surface. A thick layer of CVD nitride is then deposited on top of the oxide. The nitride is subsequently patterned and a trench is anisotropically etched into the silicon substrate. After resist stripping, the trench sidewalls are passivated with a thin layer of thermal oxide. The trenches are then filled with a thick CVD oxide and subsequently planarized using chemical-mechanical polishing (CMP), stopping on the nitride layer. Finally, the nitride barrier and pad oxide are removed.

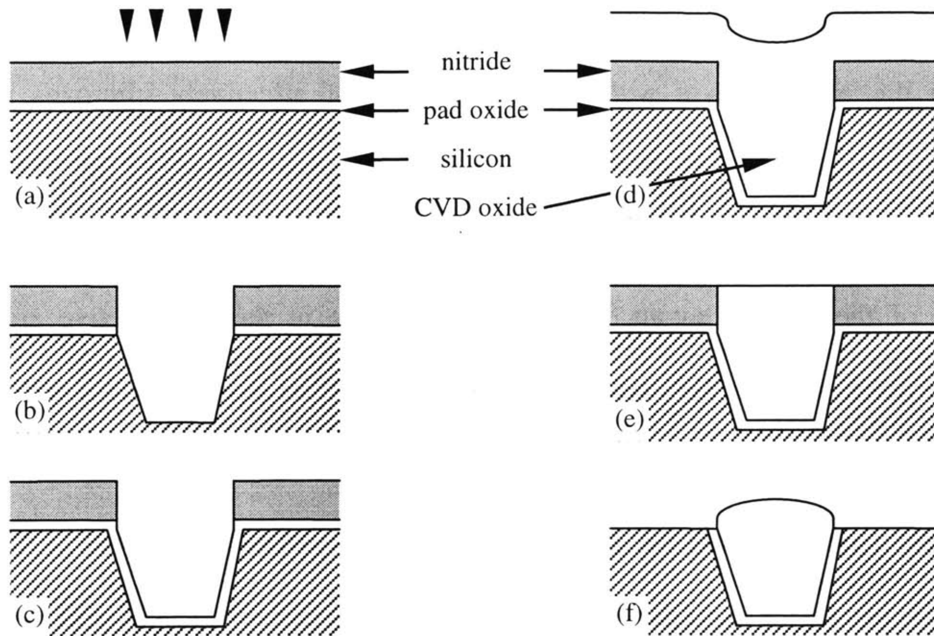

Figure 1.5 STI process flow summary: (a) pad oxide and nitride deposition, (b) anisotropic trench etch, (c) trench sidewall passivation, (d) trench fill, (e) CMP planarization, (f) nitride and pad oxide strip.

STI is able to achieve near zero field encroachment because an anisotropic etch is used to form the isolation trenches. The sidewalls are nearly vertical, and the angle of the sidewalls is limited by the trench fill capability of the oxide used [3]. The width of the isolation trenches is defined exactly by the lithography step, hence, STI can be scaled with each technology generation.

The depth of the trenches depends on the anisotropic etch process. Trenches of arbitrary depths can be fabricated by varying the etch time. Deeper trenches increase latch-up immunity, decrease junction capacitance, and decrease junction leakage [3]. In practice, the aspect ratio of the trench (ratio of height to width) is limited by the trench fill capability of the oxide used as mentioned earlier.

Several techniques have been developed to achieve planarization and most of them use CMP [1]-[3],[10]-[12]. However, the amount of material removed during CMP

depends on the pattern density of the active area [13], which causes uneven polishing within a die and across a wafer. One method that effectively improves post-CMP planarity is to use a two mask process and a combination of reactive ion etching (RIE) and CMP (reverse tone etch back) [14]. This method uses a second mask, which is a negative of the pattern layout, to remove the oxide in the large active areas which normally polish slowly. This way, uneven clearing of the oxide over the active areas is reduced.

STI appears, therefore, as the unavoidable replacement for the LOCOS-based isolation schemes for deep sub-0.5 μm technologies and beyond. STI provides a planar surface, does not suffer from field oxide thinning, and can be scaled down into smaller dimensions.

1.3 Thesis Goals

The main challenge of STI is to polish the overburden oxide controllably so that oxide removal stops once it reaches the nitride barrier. In practice, the removal rate varies within a die and across the wafer. The modeling of these variations is an important first step towards better process control. In particular, models that address pattern dependencies directly from layout are needed [4]. In this thesis, a model for reverse tone etch back for STI CMP is developed. There are currently no models for reverse tone etch back STI CMP, although models for single-step STI CMP [11] and control methods for STI CMP exist [15]. A model for reverse tone etch back for STI CMP is needed to obtain knowledge and insight that will reduce development cycle times and cost. The effects on

CMP performance due to the type of polishing pad and polishing tool are also investigated in this thesis.

1.4 Thesis Organization

This thesis is divided into five chapters. Chapter 2 introduces the CMP process and explains how pattern dependencies affect STI CMP. Reverse tone etch back is presented as an effective way to overcome uneven polishing due to variations in pattern layout.

A model for reverse tone etch back STI CMP is developed in Chapter 3. The model is an adaptation of a dual-material damascene CMP model proposed by Tugbawa [16]. The proposed model is based on the dependence of oxide and nitride removal rates on local step height. Experimental data is used to verify the modeling methodology.

An improved parameter extraction methodology using the effective density of the die instead of the designed pattern density is developed in Chapter 4. The thesis conclusions and suggestions for future work are presented in Chapter 5.

Finally, the parameter extraction routines are included in the appendices. The density averaging routines written by Ouma and later modified by Lee are used in this work, and are also included in the appendices.

Chapter 2
Chemical Mechanical Polishing for STI

Chemical mechanical polishing (CMP) is a well-known polishing process. Historically, it is used by skilled craftsmen to produce optically flat and mirror-finished surfaces. It also occurs in nature, producing beautifully finished stones. In the semiconductor industry, CMP has been used for more than 30 years to prepare silicon wafers. In recent years, CMP has emerged as the primary technique for planarizing dielectrics. It has also found wider application in the entire VLSI development and production cycle serving as an enabling tool for shallow trench isolation, damascene technologies and other novel process techniques.

In this chapter, CMP will be presented as an enabling technology for STI. Section 2.1 describes briefly the CMP process. Section 2.2 explains how CMP is used in STI and describes some of the problems encountered during CMP of STI structures, and Section 2.3 explains how reverse tone etch back solves or reduces these problems.

2.1 Overview of Dielectric CMP

The purpose of CMP in dielectric polishing is to remove topography while maintaining good uniformity across the entire wafer. CMP is very effective at reducing feature-level or local step height, and achieves a measure of global planarization not possible with spin-on and resist etch back techniques.

The schematic of a rotary CMP tool and a linear CMP tool are shown in Figures 2.1a and 2.1b respectively. CMP tools essentially comprise a polishing pad which moves relative to the wafer carrier. The wafer carrier holds the wafer face down against the polishing pad. The wafer carrier can both exert a force on the wafer and rotate the wafer independent of the polishing pad. Polishing is usually done in the presence of a polishing slurry that is fed automatically onto the polishing pad.

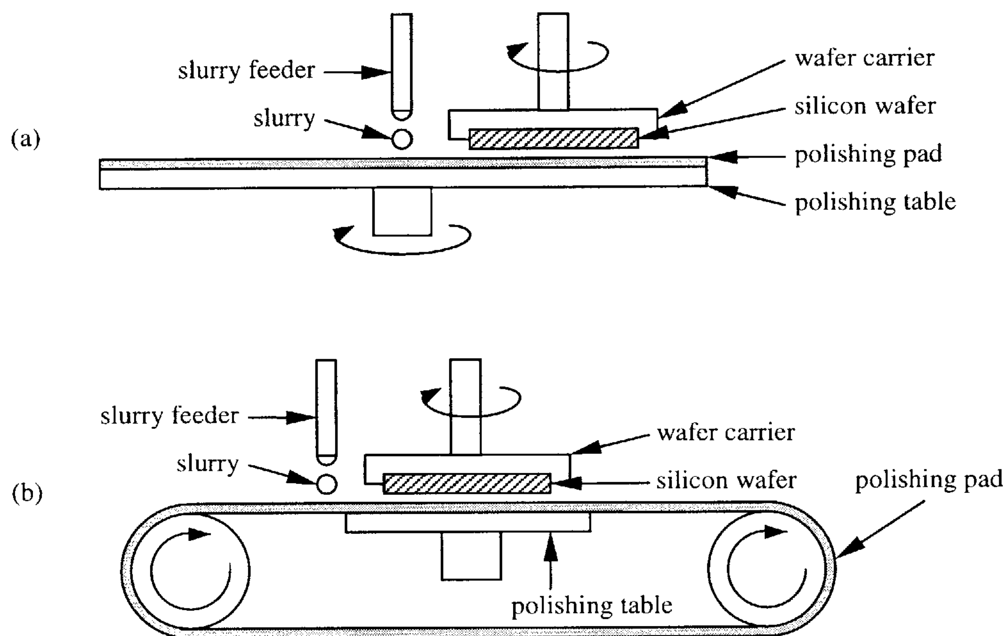

Figure 2.1 Examples of CMP tools: (a) rotary polisher, (b) linear polisher.

The exact mechanism for oxide polishing is not fully understood, and several theories exist. One such theory describes it as a chemical-mechanical mechanism at the microscopic level (Figure 2.2) involving: (1) forming hydrogen bonds between the oxide on the wafer and the slurry particles; (2) forming molecular bonds between the wafer and the slurry; and (3) breaking the oxide bonds with the wafer surface when the slurry particle moves away [8]. Hence CMP relies on chemical-mechanical action as its name

suggests, and not on mechanical abrasion. Because of the chemical effect of bond breaking, the polishing slurry has a large effect on the polishing rate. For example, slurries made from oxides with higher oxygen bond strengths such as cerium oxide, have polishing rates several times higher than silica-based slurries.

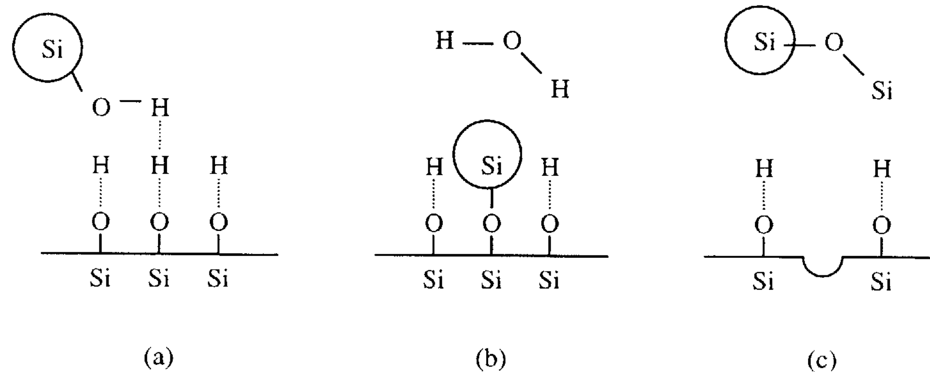

Figure 2.2 Possible oxide CMP mechanism: (a) hydrolysis of oxide surface and slurry in alkaline solution, hydrogen bond formation between the slurry and the oxide surface, (b) Si-O bond formation by releasing a water molecule, (c) removal of silicon atom when slurry particle moves away.

CMP achieves planarity due to the rigidity of the polishing pad when it is in contact with a wafer. This is illustrated in Figure 2.3. A soft pad that conforms to the topography on the surface of the wafer removes the oxide uniformly everywhere, hence it does not planarize the wafer. On the other hand, a rigid pad polishes the high spots at a faster rate, hence topography can be reduced. The rigidity of the pad depends not only on the material the pad is made from, but also on the process conditions, such as the speed of the polishing pad and the down force on the wafer.

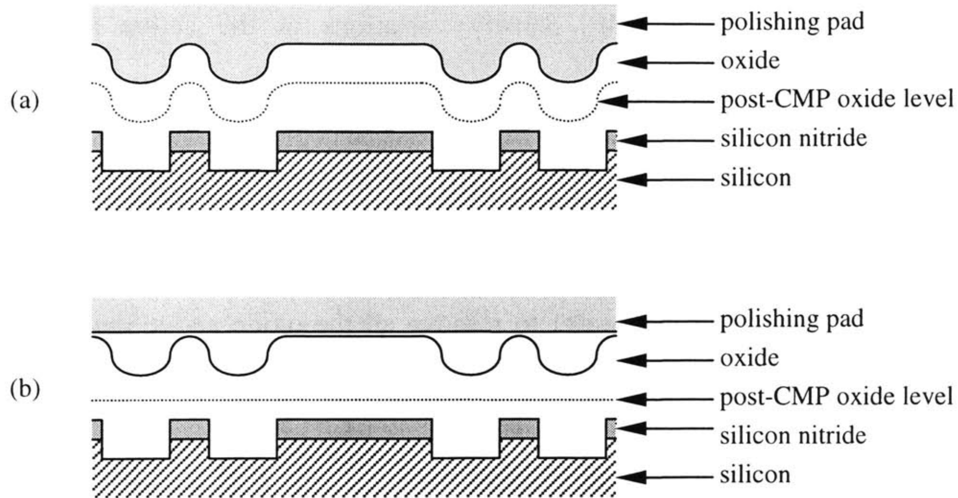

Figure 2.3 Effect of pad rigidity on planarity: (a) an ideal soft pad conforms to the initial topography and removes oxide everywhere at the same rate, (b) an infinitely rigid pad removes material in the up area faster than in the down area, so the final surface is flat.

2.2 Shallow Trench Isolation CMP

STI structures are formed using a damascene process, as shown previously in Figure 1.5. The damascene process derives its name from the traditional art of inlaying metal in ceramic or wood for decoration. Similarly, STI formation involves polishing the overburden oxide until only oxide remains in the trenches. CMP is the preferred way to remove the overburden oxide, but it is sensitive to pattern effects and process conditions.

The sensitivity of CMP to pattern density is well documented [13,19,20]. This relationship is shown explicitly in the MIT model for density-dependent polish rate [19]:

$$Rate = \frac{K}{\rho} \tag{2.1}$$

where K is the blanket removal rate and ρ is the density of the up area.

In conventional STI CMP, density variations in the active area cause the overburden oxide above the low density nitride regions to be removed faster than the oxide above the high density nitride regions. As shown in Figure 2.4a, the nitride in the low density regions will be cleared earlier than the nitride in the high density regions. It is thus necessary to overpolish the wafer to remove all the oxide above the nitride, as any oxide that remains above the nitride will prevent the nitride from being completely stripped off during the subsequent processing steps.

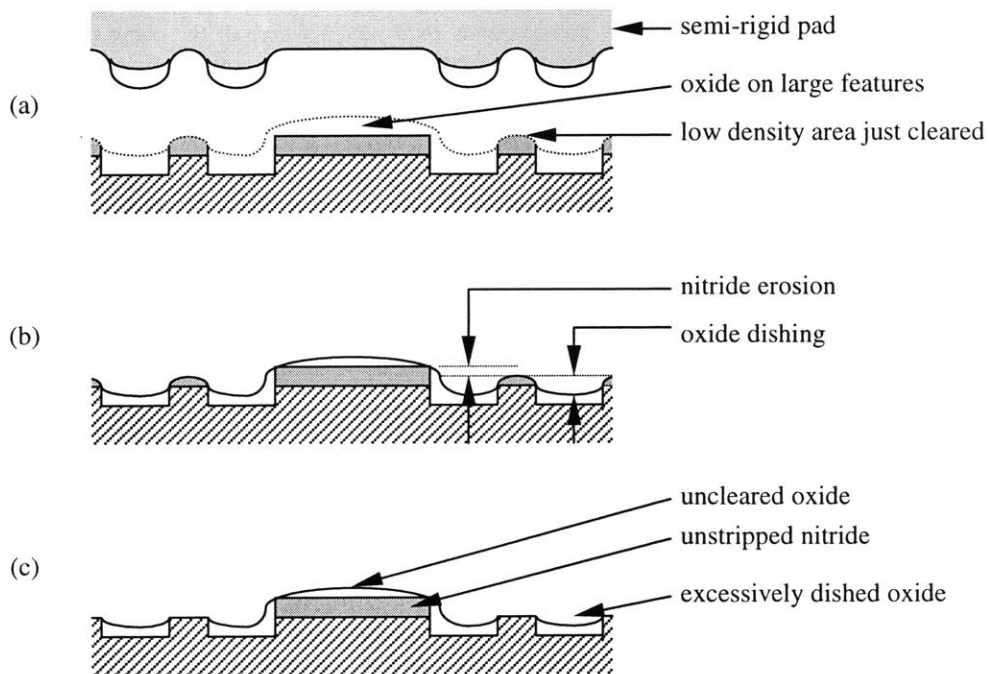

Figure 2.4 Problems with conventional STI CMP: (a) a realistic semi-rigid pad polishes oxide at different rates depending on the pattern density, (b) nitride erosion and oxide dishing due to uneven polishing, (c) any oxide that is left on top of the nitride prevents nitride stripping; overpolishing can cause the oxide to recess below the silicon.

There are two undesirable consequences of overpolishing: oxide dishing and nitride erosion. Oxide dishing is said to occur when the top of the oxide in the trenches recesses below the top of the nitride as shown in Figure 2.4b. Dishing occurs partly

because the slurry is normally chosen so that the oxide polishes faster than the nitride. Since the polishing pad is not infinitely rigid, it is able to deform into the trenches as the oxide in the trenches is removed faster than the nitride in the up areas. Hence, dishing increases the amount of topography present in a die. Overpolishing can also cause the oxide to recess below the silicon as shown in Figure 2.4c. This is undesirable because it degrades the quality of the isolation and may damage the edges of the silicon active area. Nitride erosion occurs in the overpolished regions because the extra amount of polishing causes some nitride to be removed. Thinning of the nitride layer due to erosion is a problem because it may cause the underlying silicon active area to be damaged by CMP.

2.3 Reverse Tone Etch Back STI

Dishing and erosion can be reduced by using an additional photolithography and RIE etch step prior to CMP. The additional process steps are shown in Figure 2.5. After depositing the overburden oxide, the oxide is patterned using a reverse tone mask. The reverse tone mask is basically an inverse of the mask used to pattern the wafer to form the STI structures. Some slight biasing is applied to account for overlay errors. Hence, the reverse tone mask defines the area of oxide above the nitride that will be removed. The exposed oxide is removed using an RIE etch that stops on nitride. Finally, the excess oxide in the trenches is removed using CMP.

The purpose of the reverse tone etch back step is to remove most of the overburden oxide above the nitride, especially the oxide in the large nitride areas which are difficult to remove during conventional STI CMP. Hence, the CMP step is now concerned only with removing the excess oxide in the trenches to reduce topography.

However, the removal of the excess oxide is still density dependent and some regions will polish faster than others. Fortunately, the requirements for this are less stringent (than requiring that all the oxide above the nitride be removed), thus the amount of overpolishing can be reduced. This helps to reduce dishing. Unfortunately, because the nitride is already exposed prior to CMP, this process may increase the amount of nitride erosion. This can be solved by using slurries with higher oxide to nitride selectivity.

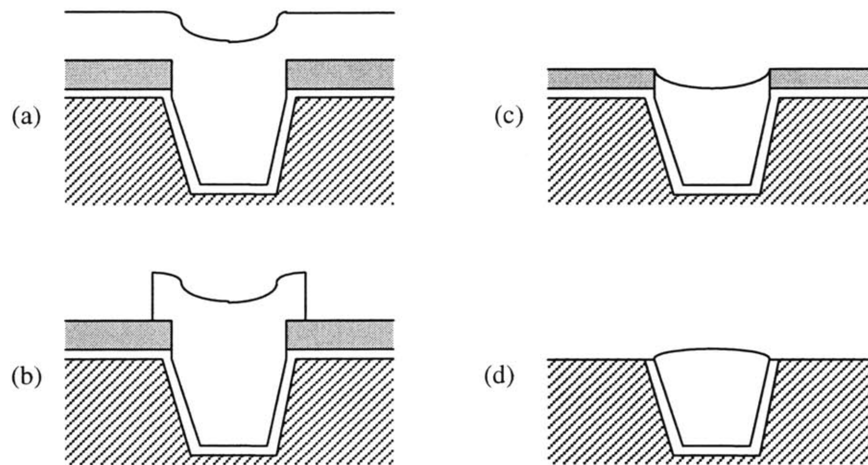

Figure 2.5 Modified process flow for reverse tone etch back STI CMP: (a) cross-section of STI structure after oxide deposition, (b) reverse tone etch back of most of the overburden oxide above the nitride area, (c) post-CMP profile showing dishing and erosion, (d) nitride and pad oxide strip.

The reverse tone etch back process is expensive because it requires an additional photolithography step. Several other methods of planarizing the wafer prior to CMP have been proposed, such as using dummy fill [1,17], selective oxide deposition [12], and spin-on films [18]. However, reverse tone etch back is still commonly used because it is the most effective in reducing the post-CMP difference in step height between small and large active areas [1].

Chapter 3
Modeling of Reverse Tone Etch Back STI CMP

Shallow trench isolation (STI) is an enabling process for advanced ULSI technologies. It can be scaled to fine dimensions while maintaining good planarity, good latch-up immunity, and low junction capacitance. However, the CMP process is density dependent and single-step STI CMP can lead to significant oxide dishing and nitride erosion problems. Hence, an additional etch back step is commonly used before CMP to remove the overburden oxide over large active areas. The resulting CMP process is concerned only with removing the excess oxide in the trenches until the oxide reaches the same level as the nitride. This is a complicated process that depends on the relative removal rate of the oxide in the trenches and the nitride barrier in the raised area, as well as the pattern density. There are currently no existing models for reverse tone etch back STI CMP, even though models for single-step STI CMP and process control methods exist. In this chapter, a mathematical model for reverse tone etch back STI CMP based on density and step height dependent oxide and nitride removal rates is presented.

Some previous work on CMP modeling is presented in Section 3.1. The reverse tone etch back STI CMP model is described in detail in Section 3.2. Section 3.3 explains how the equations for step height (or dishing) and nitride erosion are derived from the model. Section 3.4 describes the experiments and the STI characterization mask used to pattern the wafers that are used in this modeling work. The method for extracting the

model parameters is explained in Section 3.5. The model and actual measurements are compared in Section 3.6. Additional modeling results are shown in Section 3.7.

3.1 Previous Work

The model presented here is a culmination of previous work performed at the Massachusetts Institute of Technology: Stine *et al.* demonstrated the strong relationship between CMP removal rate and pattern density [19], Smith *et al.* described integrated pattern density and step height models for oxide CMP [20], and Tugbawa *et al.* proposed a removal rate vs. step height model for dual-material damascene CMP [16].

3.1.1 Density Dependent CMP Model

The basic MIT density model for dielectric CMP provides a first-order approximation of post-polish dielectric thickness for arbitrary layouts [19]-[21]. The model is derived from Preston's equation, and assumes that the polishing rate of a raised area is equal to the blanket rate divided by its effective density as shown in equation (2.1). However, the model assumes that no down area polishing occurs until the local step height is removed. Once the step height is removed, the model assumes that the removal rates of both the raised and down areas equal the blanket rate.

Grillaert *et al.* found that, for small step heights, polish occurs in both up and down areas, in contrast to up area contact only for large steps [22]. Based on this effect, Smith *et al.* improved the density based polish model by combining effective density and time dependencies which take into account the time at which the pad contacts the down

areas. Using this methodology, Smith demonstrated a 50% improvement in fit to experimental data over the original density model.

3.1.2 Removal Rate vs. Step Height CMP Model

Tugbawa *et al.* proposed a dual-material damascene CMP model based on the relationship between removal rate and step height during CMP [16]. The model incorporates the following key observations used by Smith. (1) Polishing pads are not infinitely hard and may deform into a space, and the step height at which the pad contacts the down area, d_{max}, is determined by the properties of the pad and pattern density [20,21,22]. (2) For step heights larger than d_{max}, the up areas polish at a rate given by the MIT density model. (3) For step heights smaller than d_{max}, the up area removal rate decreases with decreasing step height while the down area removal rate increases with decreasing step height. (4) Changes in step height cease once the up area removal rate becomes the same as the down area removal rate. Tugbawa captured these observations into a removal rate vs. step height plot, from which equations describing dual-material CMP can be derived.

The removal rate vs. step height model also unifies several observations from other CMP models: (1) Burke proposed that step height decreases exponentially with time [23]; (2) Tseng *et al.* proposed that the removal rates of raised and down areas converge exponentially to the blanket removal rate as polish time increases [24]; (3) the IMEC model proposed that step height at which the pad contacts the down area is a function of the feature density [22].

The removal rate vs. step height model should work for any CMP process, but it is extremely useful for modeling damascene processes like copper CMP or STI CMP, where simultaneous polishing of more than one material is involved. The reverse tone etch back STI CMP model presented here is an adaptation of Tugbawa's dual-material damascene CMP model, which greatly simplifies the analysis of reverse tone etch back STI CMP into a simple graph as shown in the next section.

3.2 Model Formulation

Chemical mechanical polishing (CMP) as its name suggests, achieves global planarity through a combination of chemical action from the slurry and mechanical action from the polishing pad and slurry particles. The slurry chemistry can be adjusted for varying degrees of selectivity between different materials, but the contact between the polishing pad and the wafer is the main mechanism for removing the local step height that causes planarization. In STI CMP, we are interested in changes in step height (especially dishing) and nitride erosion. This makes a step height based model a convenient starting point. Furthermore, when analyzing step height changes, we do not overload ourselves with the details of the physical or chemical aspects of CMP. Instead, we take a broader perspective of the sum of all contributing factors. From the measurement point of view, changes in local step height are also easier to measure.

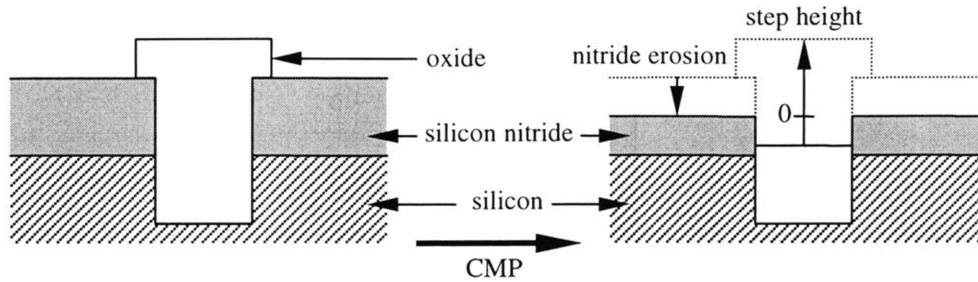

Figure 3.1 Cross-section of a reverse tone etch back STI structure showing nitride erosion and step height after CMP.

Before delving into the model, we first define step height (dishing) and nitride erosion as shown in Figure 3.1. Figure 3.1 shows the cross section of a reverse tone etch back wafer before and after CMP. The local step height is the vertical distance between the top of the nitride and the top of the oxide. It is positive when the oxide is above the nitride, and negative when the oxide recesses below the nitride. Negative step height is also known as dishing. Nitride erosion is simply the amount of nitride loss due to CMP.

As shown, the reverse tone etch back process leaves a narrow region of oxide remaining on the nitride up areas. The amount of overlap depends on the design of the reverse tone etch back mask. For this work, the overlap is measured to be 0.2 μm. For nitride widths greater than 8 μm, the overlap reduces the exposed nitride area by less than 10%, based on a square active area. Hence, in this work, we assume that the area of the exposed nitride is approximately the designed area since features with much larger dimensions are used.

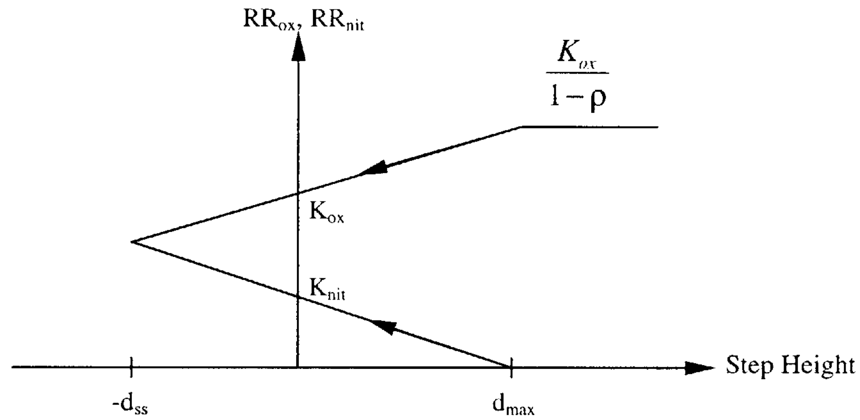

Figure 3.2 Removal rate vs. step height model for reverse tone etch back STI CMP.

The model can be explained graphically in Figure 3.2, which shows how the oxide and nitride removal rates on a reverse tone etch back STI wafer change with step height. The vertical axis measures the oxide removal rate in the STI trenches (RR_{ox}), and the nitride removal rate in the active areas (RR_{nit}). The horizontal axis measures the local step height. From the way the graph is drawn, we can infer that polishing progresses from the right to the left of the graph (from positive step height to negative step height) as indicated by the arrows. The graph with the upper arrow is for oxide CMP, and the one with the lower arrow is for nitride CMP.

As mentioned earlier, this model recognizes that polishing pads are not infinitely hard. When a pad is in contact with a wafer, it is supported mostly by the up areas of the wafer. However, the pad also deforms into the spaces between the up areas. If the local step height is very high, the pad will not contact the down area, and there will be no down area polishing. The up area (oxide) polish rate in this case is density dependent and given by the expression $RR_{ox} = \frac{K_{ox}}{1-\rho}$, where K_{ox} is the blanket oxide removal rate, and ρ is the nitride density.

As the wafer polishes, only the oxide in the up areas are removed and this causes the local step height to decrease. At some critical step height denoted by d_{max}, the pad just touches the down area (nitride). The pad is now supported by both the up and down areas. The down area removal rate is now non-zero. Additional polishing further reduces the local step height which increases the force of contact between the pad and the down area while it decreases the force between the pad and the up area. This causes the down area removal rate to increase and the up area removal rate to decrease. For simplicity, the model assumes that the down area removal rate increases linearly and the up area removal rate decreases linearly with decreasing step height as shown in Figure 3.2. This is verified experimentally.

When the local step height is zero, we postulate that the down area removal rate is equal to K_{nit}, the blanket nitride removal rate. Similarly, the up area polish rate is equal to K_{ox}, the blanket oxide removal rate. Ideally, we want to stop polishing at this point since we have removed the local step height as desired. In reality, different points on a wafer achieve local planarity at different times. Hence, overpolishing is necessary, and this causes the oxide to recess below the nitride. When the oxide recesses below the nitride, we say that dishing has occurred. As long as the oxide removal rate is higher than the nitride removal rate, the amount of dishing increases with polish time. Eventually, the oxide removal rate and nitride removal rate become equal and steady-state dishing occurs. We denote this point by d_{ss} in Figure 3.2.

3.3 Mathematical Relations

Figure 3.2 contains all the information needed to completely model the reverse tone etch back STI CMP process. In fact, the model can be described completely using only four variables: the density-independent oxide removal rate (K_{ox}), the density-independent nitride removal rate (K_{nit}), the effective pattern density ρ, and the pad deformation limit (d_{max}). The graphs in Figure 3.2 can be described mathematically as follows:

$$\textit{Oxide Removal Rate, } RR_{ox} = \begin{cases} \dfrac{K_{ox}}{1-\rho} & H > d_{\max} \\ K_{ox}\left(1+\dfrac{\rho}{1-\rho}\dfrac{H}{d_{\max}}\right) & -d_{ss} < H < d_{\max} \end{cases} \tag{3.1}$$

$$\textit{Nitride Removal Rate, } RR_{nit} = \begin{cases} 0 & H > d_{\max} \\ K_{nit}\left(1-\dfrac{H}{d_{\max}}\right) & -d_{ss} < H < d_{\max} \end{cases} \tag{3.2}$$

where H is the step height. Using these equations, the following useful relations can be derived.

3.3.1 Steady State Dishing

The amount of steady state dishing is the maximum distance the oxide in the trenches can recess below the nitride. In STI CMP, we want the level of the post-CMP oxide to be above the silicon. Thus the amount of steady state dishing determines the minimum nitride thickness required, assuming no nitride loss during CMP. By definition, steady state dishing occurs when the oxide and nitride removal rates are equal. Equating equations (3.1) and (3.2), the expression for steady state dishing is

$$d_{ss} = \frac{\left(K_{ox} - K_{nit}\right)\left(1-\rho\right) d_{\max}}{\left(1-\rho\right) K_{nit} + \rho\, K_{ox}} \tag{3.3}$$

3.3.2 Step Height

Ideally, polishing should stop when the features are planar, that is, when the local step height is zero. The amount of polishing required can be easily calculated if the time evolution of step height is known. The rate of change of step height is given by the difference in the oxide removal rate and the nitride removal rate:

$$\frac{dH}{dt} = RR_{ox} - RR_{nit} \tag{3.4}$$

Integrating this gives the expression for step height:

$$H(t) = \begin{cases} d_0 - \dfrac{K_{ox}}{\rho} t & H > d_{\max} \\ d_{\max} - \left(d_{ss} + d_{\max}\right)\left(1 - e^{-\frac{t - t_c}{\tau}}\right) & H < d_{\max} \end{cases} \tag{3.5}$$

where the exponential time constant τ and the touch down time t_c are given by:

$$\tau = \frac{d_{\max}(1-\rho)}{(1-\rho)\, K_{nit} + \rho\, K_{ox}} \tag{3.6}$$

$$t_c = \frac{\left(d_0 - d_{\max}\right)(1-\rho)}{K_{ox}} \tag{3.7}$$

The exponential time constant, τ, is a measure of how fast a given process can achieve planarity. The touch down time, t_c, is the amount of polishing required before the pad contacts the down areas. The local step height before CMP is given by d_0. The above expressions are valid in general, but if $d_0 < d_{max}$, we can simplify equation (3.5) to:

$$H(t) = d_0 - \left(d_{ss} + d_0\right)\left(1 - e^{-\frac{t}{\tau}}\right) \tag{3.8}$$

3.3.3 Nitride Erosion

The nitride layer is used as a barrier layer to protect the underlying silicon from damage during CMP. Ideally, the nitride removal rate is zero. In practice, depending on the process used, nitride loss can be significant. The amount of nitride loss during CMP determines the amount of overpolishing that can be tolerated and the thickness of the nitride layer needed. The expression for nitride erosion can be similarly derived by integrating the nitride removal rate:

$$\frac{dE_{nit}}{dt} = RR_{nit} \tag{3.9}$$

$$E_{nit}(t) = \begin{cases} 0 & H > d_{\max} \\ \dfrac{K_{ox}\ K_{nit}}{(1-\rho)\ K_{nit} + \rho\ K_{ox}}\, t - \dfrac{K_{nit}(d_{ss}+d_0)(1-\rho)}{(1-\rho)\ K_{nit} + \rho\ K_{ox}}\left(1 - e^{-\frac{t-t_c}{\tau}}\right) & H < d_{\max} \end{cases} \tag{3.10}$$

Similarly, if $d_0 < d_{max}$, we can simplify equation (3.10) to:

$$E_{nit}(t) = \frac{K_{nit}\ K_{ox}}{(1-\rho)\ K_{nit} + \rho\ K_{ox}}\, t \ - \ \frac{K_{nit}(d_{ss}+d_0)(1-\rho)}{(1-\rho)\ K_{nit} + \rho\ K_{ox}}\left(1 - e^{-\frac{t}{\tau}}\right) \tag{3.11}$$

3.4 Experimental Details

Several STI CMP experiments were performed to validate the reverse tone etch back STI CMP model that was presented in the previous section. The effect of pattern density, type of polishing pad, and type of polishing tool on step height and nitride erosion were investigated.

3.4.1 The STI CMP Characterization Mask

The STI CMP characterization mask set is designed for CMP consumable, process, and tool characterization and evaluation. Its design is based loosely on the MIT CMP characterization mask. Each mask is designed to produce a 21.095 mm $\times$ 21.095 mm die. The first mask is the positive mask, and is made up of STI structures and sample devices arranged as shown in Figure 3.4. Figure 3.3a shows a close up of the positive mask. The dark squares in the clear field mask represent where the silicon is not etched, so that vertical posts with square cross-sections to emulate STI structures are formed. The length of the active areas (x) and the "width" of the trenches (y) are indicated as shown. Within each cell on the mask, the active area lengths and trench widths are the same.

The second mask (Figure 3.3b) is a dark-field mask which is a negative of the positive mask, except that (1) STI structures with active area lengths less than or equal to 1 μm are not reproduced; (2) a negative bias of 0.2 μm is applied to the remaining structures. Hence, only the nitride above the large active areas are exposed after etch back. Since the area of nitride that is exposed after etch back is generally large compared

to the area of the oxide remaining on the active areas due to biasing, the density of the exposed nitride can be approximated by the designed pattern density.

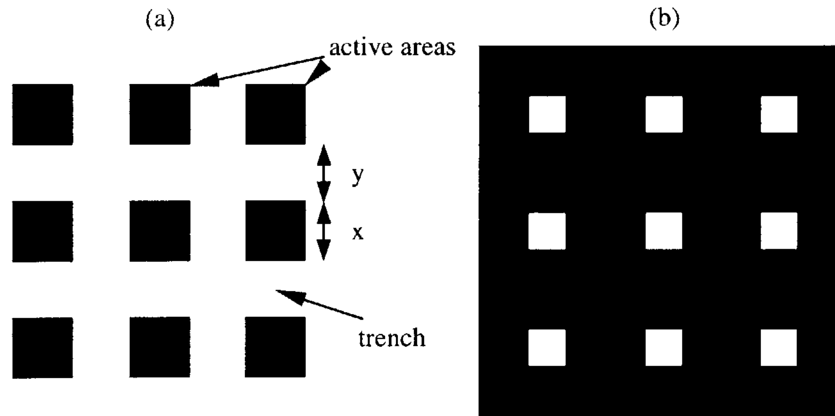

Figure 3.3 Close-up of STI CMP characterization masks: (a) positive mask used to define the STI structures, (b) reverse tone mask used to pattern the oxide for etch back.

Figure 3.4 shows a schematic of the STI CMP characterization mask. There are altogether 36 cells, and the active area length and trench width of the STI structures in each cell are indicated as shown, e.g., 1/500 indicates a 1 μm active area length and 500 μm trench width. The structures in rows 4, 5, and 6 have active area lengths of 100 μm, 1 μm, and 0.4 μm respectively, while the trench width varies from 1000 μm to 0.25 μm from column A to F as shown. Cells 1A, 1B, 2A, and 2B are similarly designed. These cells can be used to study the effects of active area size and trench width on polishing. Cells 1aC, 1bC, 2aC, and 2bC are fine pitch structures, where $x = y$ in each cell, but the pitch (defined as $x + y$) varies from 0.5 μm to 2 μm. Together with cells 4C and 5E, they can be used to investige the effect of pitch on polishing. Cells D1, D2, and E1 contain sample patterns from a flash memory, SRAM, and logic circuit respectively. They can be used to compare the results from polishing the emulated STI structures to those from real-

life structures. Cell F1 consists of 7000 Å long lines in varying line width and line space combinations. It is designed for studying the trench fill capabilities of the deposited oxide.

Of particular interest in this work are the step density structures along row 3. The pitch in these structures is 80 μm while the active area lengths and trench widths vary to produce pattern densities that range from 10% to 75%. We define density as

$$\rho = \left(\frac{x}{x+y} \right)^2 \tag{3.12}$$

The difference in density between adjacent cells is designed to be large to better capture density averaging effects during polishing [21].

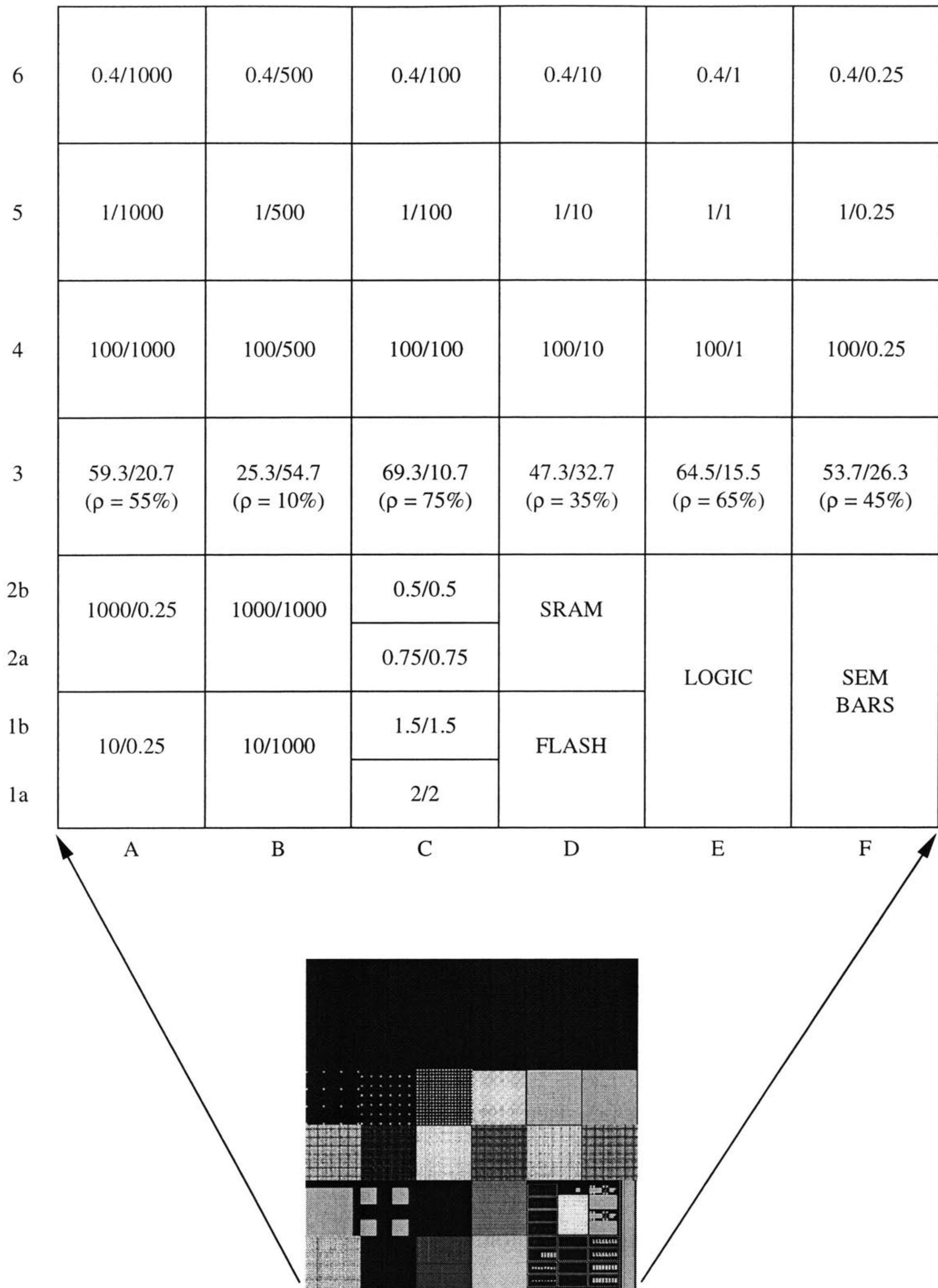

Figure 3.4 Schematic of STI CMP characterization mask showing the combination of active area lengths and trench widths

3.4.2 Process Conditions

Nineteen STI wafers were prepared by first growing 90 Å of pad oxide, followed by depositing 1000 Å of CVD silicon nitride, and finally depositing 320 Å of silicon oxynitride (SiON) onto bare silicon wafers. The wafers were then patterned using the positive mask. Subsequently, the wafers were anisotropically etched until trenches with a depth of 3500 Å in silicon were formed. 7000 Å of HDP oxide was then deposited and sputter-etched back to 5800 Å. Following this, the wafers were patterned using the reverse tone mask, and the oxide in the large active areas was etched back to expose the nitride.

Table 3.1 summarizes the three different CMP processes used to polish the wafers. Seven wafers were polished using process A, which used the IC1000/SubaIV stacked polishing pad on the Applied Materials Mirra polisher. Seven wafers were polished using process B, which also used the Mirra tool but with an IC1000/Solo hard polishing pad. Five wafers were polished using process C, which used the IC1000/TW817 polishing pad (which is similar to the IC1000/Solo pad) on a Lam Research Teres linear polisher. Processes A and B polished wafers using 63 rpm platen speed, 57 rpm head speed, and 2.8 psi pressure. Process C used 125 fpm belt speed and 7 psi pressure. All three processes used standard silica-based SS-25 slurry with 1:1 dilution in DI water. The choice of these three processes allows us to compare the effects of pad type and tool type on dishing and erosion.

Wafers in each process were polished for varying amounts of time. Oxide thickness in the trenches and nitride thickness in the exposed active areas were measured before and after CMP using optical film thickness measurement tools such as the

Nanospec 8000 or the KLA Tencor UV1280. Measurements were taken from the center die of each wafer, and from the center of each cell in the step density region, resulting in 12 measurements per wafer.

Table 3.1 Summary of CMP Conditions

Process	Wafer Number	Type of Polisher	Type of Polishing Pad	
A	1 - 7	Rotary	IC1000/Suba IV	(Stacked Pad)
B	8 - 14	Rotary	IC1000/Solo	(Hard Pad)
C	15 - 19	Linear	IC1000/TW817	(Hard Pad)

3.5 Parameter Extraction Methodology

The model parameters can be extracted by minimizing the sum-squared error between the model and the measurement data for each process. Although five variables are used in the model, only three are required to completely model each process: K_{ox}, K_{nit}, and either τ, d_{ss} or d_{max}, assuming we know ρ from the layout. In this work, K_{ox}, K_{nit}, and τ are used. From these variables, the values of d_{ss} and d_{max} can be calculated:

$$d_{ss} = \tau \left(K_{ox} - K_{nit} \right) \quad (3.13)$$

$$d_{\max} = \tau \frac{\left(1-\rho\right) K_{nit} + \rho K_{ox}}{\left(1-\rho\right)} \quad (3.14)$$

For each process, K_{ox} and K_{nit} are independent of polish time or pattern density, whereas τ is a function of density.

In this work, we assume initially that $d_0 < d_{max}$ so we can use the simplified expressions for step height and nitride erosion in equations (3.8) and (3.11). We will show later that this assumption is valid. From equations (3.8) and (3.11), we can express the local step height $H_i(t_j)$ and the amount of nitride erosion $E_i(t_j)$ for each density region i and polish time t_j in terms of the chosen variables:

$$\begin{cases} H_i(t_j) = d_{0i} - \left(\tau_i \left(K_{ox} - K_{nit}\right) + d_{0i}\right)\left(1 - e^{-\frac{t_j}{\tau_i}}\right) \\ \\ E_i(t_j) = \dfrac{K_{ox}\ K_{nit}}{\left(1-\rho_i\right) K_{nit} + \rho_i\ K_{ox}} t_j - \dfrac{\tau_i\ K_{nit}\left(K_{ox} - K_{nit}\right)\left(1-\rho_i\right)}{\left(1-\rho_i\right) K_{nit} + \rho_i\ K_{ox}}\left(1 - e^{-\frac{t_j}{\tau_i}}\right) \end{cases} \tag{3.15}$$

where the densities ρ_i are initially taken to be equal to the designed pattern densities. This assumes that the planarization length for each process is small or comparable to the size of each density block (3.5 mm × 3.5 mm).

Using the experimental CMP data, the values of K_{ox}, K_{nit} and τ_i are obtained by minimizing concurrently the sum-squared error for step height and nitride erosion:

$$\underset{K_{ox}, K_{nit}, \tau_i}{\arg\min} \quad \sum_{j=1}^{J} \sum_{i=1}^{I} \left\{ \left[H_i(t_j) - h_i(t_j)\right]^2 + \left[E_i(t_j) - e_i(t_j)\right]^2 \right\} \tag{3.16}$$

where I = 6 is the number of structures measured on each die, and J = 7 (processes A and B) or 5 (process C) is the number of wafer time splits considered. For each process, we thus have I × J = 42 (processes A and B) or 30 (process C) total measurements which we

use to fit I + 2 = 8 model parameters. The quality of the fit is determined by calculating the root-mean-square (RMS) errors between the model and the experimental data for step height and nitride erosion.

3.6 Results and Discussion

A model for reverse tone etch back STI CMP is proposed and the parameters that completely describe dishing and nitride erosion are extracted. The extracted values of K_{ox}, K_{nit} and τ for each process are shown in Table 3.2, and the corresponding RMS errors for step height and nitride erosion are summarized in Table 3.3. With a few exceptions, the RMS errors obtained are less than 50Å. Hence, the results show that the model fits the experimental data with good confidence. Plotting the model and measurement points for step height for each process in Figures 3.5, 3.6 and 3.7 further verifies that the model does indeed have the correct shape. Finally, Table 3.2 shows that the extracted values for d_{max} are larger than the measured initial step height (except the 10% and 35% density regions, process C). Hence the initial assumption that $d_0 < d_{max}$ is valid. The results are discussed in detail next.

Table 3.2 Summary of results from the parameter extraction. The d_{ss} and d_{max} values shown here are derived from the extracted K_{ox}, K_{nit}, and τ parameters.

	Process A	**Process B**	**Process C**
K_{ox} (Å/min)	848	771	2189
K_{nit} (Å/min)	228	207	628
Selectivity	3.72	3.72	3.49

Density (%)	**τ (min)**	**d_{ss} (Å)**	**d_{max} (Å)**
Process A			
10	9.29	5760	2993
35	5.28	3271	3611
45	3.78	2341	3480
55	3.06	1895	3864
65	2.22	1378	4007
75	1.50	928	4150
Process B			
10	7.68	4325	2250
35	4.97	2798	3092
45	4.63	2607	3878
55	3.59	2020	4121
65	2.72	1533	4459
75	1.74	982	4394
Process C			
10	1.02	1599	722
35	0.65	1022	1195
45	0.65	1010	1572
55	0.55	853	1842
65	0.52	813	2500
75	0.38	593	2917

Table 3.3 RMS errors for step height and nitride erosion.

Density (%)	Process A		Process B		Process C	
	Step Height RMS Error (Å)	Nitride Erosion RMS Error (Å)	Step Height RMS Error (Å)	Nitride Erosion RMS Error (Å)	Step Height RMS Error (Å)	Nitride Erosion RMS Error (Å)
10	43.5	65.3	52.2	91.9	115.8	130.1
35	24.4	32.8	43.9	43.2	19.4	57.2
45	25.0	37.3	34.8	47.6	52.9	48.1
55	24.0	37.3	44.9	41.3	23.8	61.2
65	18.2	43.4	31.6	48.5	44.8	60.7
75	51.6	47.4	68.6	50.6	17.4	82.1

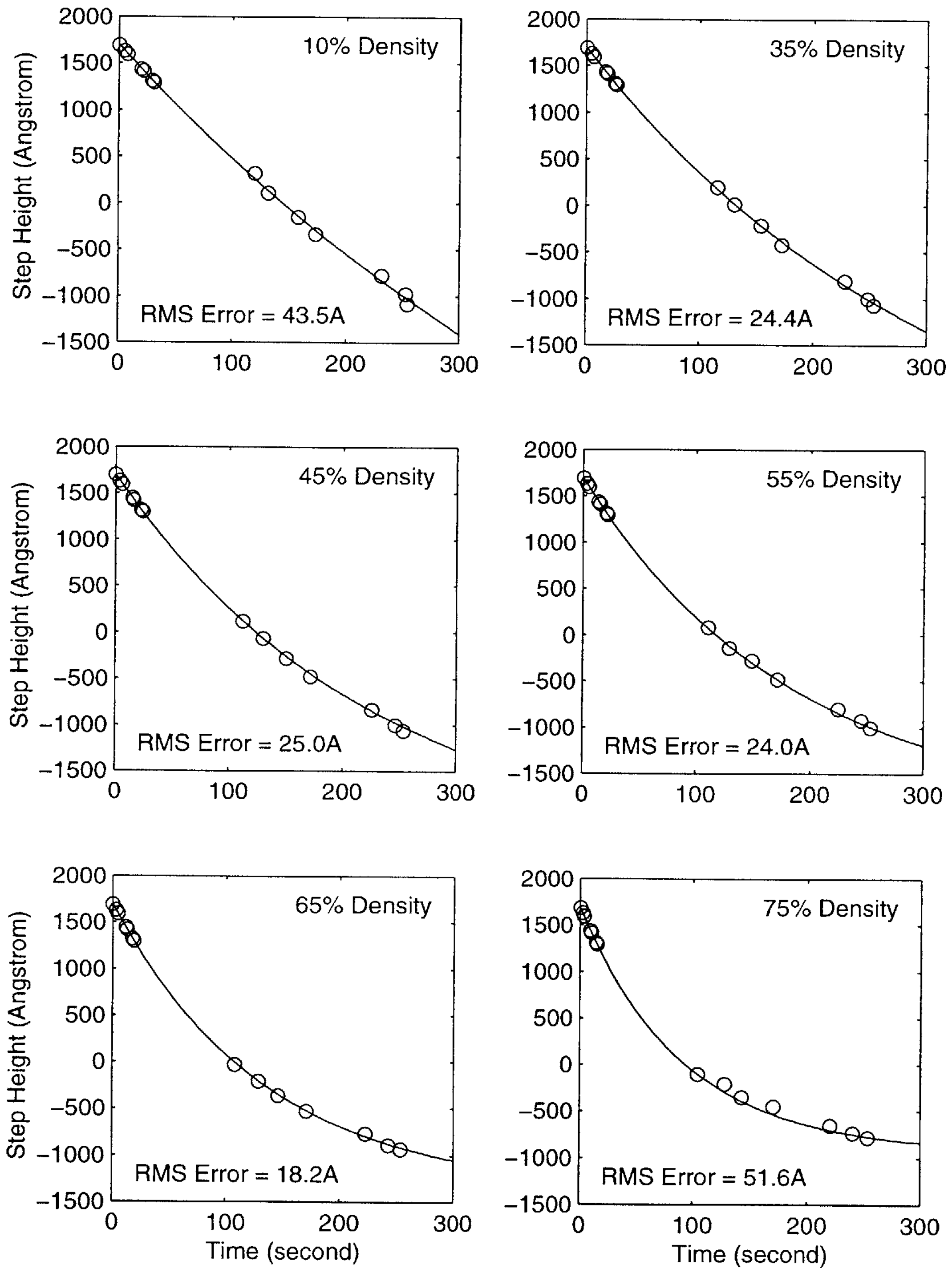

Figure 3.5 Actual (circles) and predicted step height (lines) for process A.

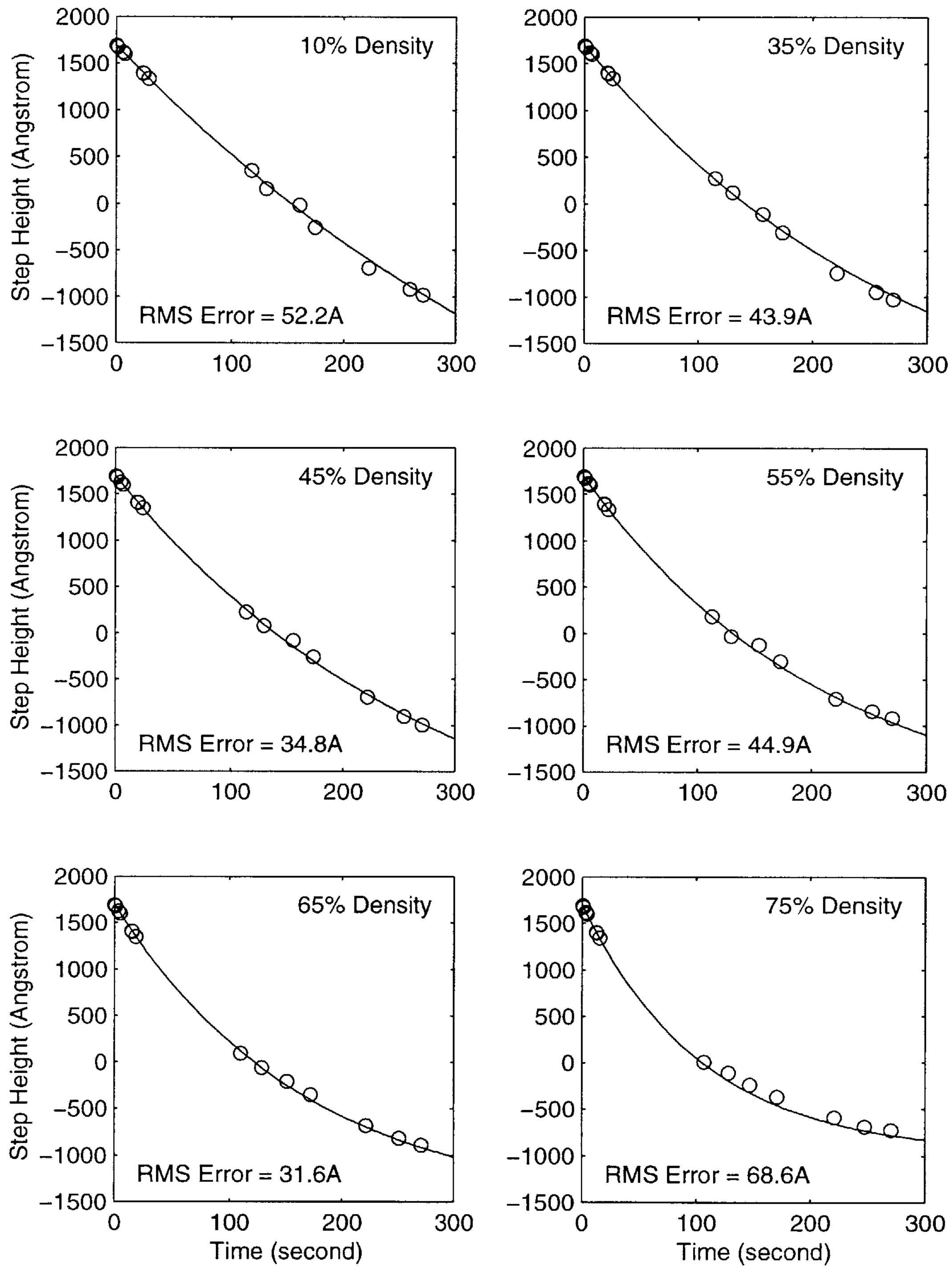

Figure 3.6 Actual (circles) and predicted step height (lines) for process B.

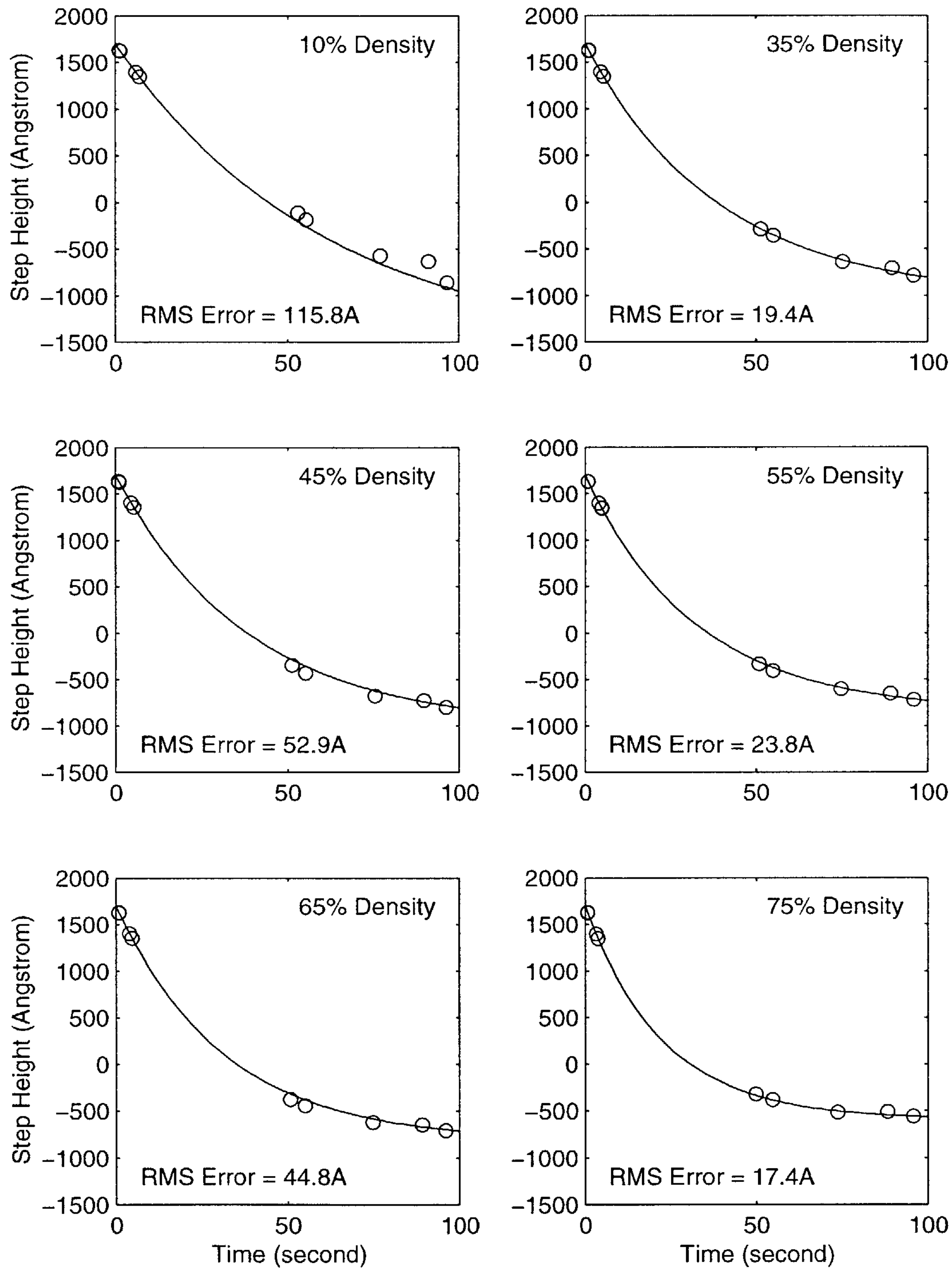

Figure 3.7 Actual (circles) and predicted step height (lines) for process C.

3.6.1 Oxide-Nitride Selectivity

The oxide-nitride selectivity is a measure of how much faster the oxide polishes compared to the nitride. The selectivity is a function of step height, as shown in Figure 3.2. Hence, it is defined here as the ratio of the density-independent removal rates:

$$Selectivity = \frac{K_{ox}}{K_{nit}} \quad (3.17)$$

The selectivity for each process is shown in Table 3.2. The selectivity is the same for process A and B and only slightly smaller for process C. It seems that selectivity depends very weakly on the pad or tool type. One possible explanation is that selectivity is largely a chemical effect, that is, it depends on the type of slurry used. Since only one type of slurry is used, all three processes have roughly the same selectivity as expected. However, the selectivity for all three processes is higher than the selectivity obtained by polishing blanket oxide and nitride wafers using the same processes. For example, the selectivity obtained using the latter method ranges from 2.4 to 2.8, but the extracted values are much higher (3.49 to 3.72).

3.6.2 Polish Time Constant, τ

The dependence of τ on pattern (nitride) density and process is shown graphically in Figure 3.8a. It shows that τ decreases with increasing density. Since τ is a measure of how fast planarization occurs, this shows that structures with higher pattern density achieve planarity faster. This appears correct because the oxide removal rate is inversely

proportional to oxide density so in the large pattern density areas (small oxide density), the oxide removal rate is high. Figure 3.8a also shows that process C has the smallest values for τ regardless of density.

The rate at which τ changes with density can be examined by normalizing τ for each process to the value of τ when the density is 10% as shown in Figure 3.8b. The graphs show that process C is the least sensitive to density variations.

3.6.3 Steady State Dishing, d_{ss}

Figure 3.8c shows the dependence of d_{ss} on density and process. The graphs have the same shape as those for τ, since $d_{ss} = \tau\left(K_{ox} - K_{nit}\right)$ as shown in equation (3.13). Recall that d_{ss} is the maximum amount the oxide in the trenches can recess below the nitride when the wafer is overpolished. This depends inversely on the amount of up area (nitride) that is supporting the polishing pad. In the high density areas, most of the pad is supported by the up areas, so d_{ss} is small as expected. Conversely, d_{ss} is large in the low density areas.

The amount of steady-state dishing also depends on the rigidity of the polishing pad. Because rigid pads are less pliant than less rigid pads, they are able to deform less into the oxide trenches (while being supported by the nitride up areas). As discussed earlier in Chapter 2, pad rigidity is probably affected by the type of polishing pad and the process conditions. Figure 3.8c shows that process A (stacked pad) and process B (hard pad) have similar d_{ss} even though different types of polishing pad are used. This suggests that d_{ss} does not depend strongly on the type of polishing pad. In addition, d_{ss} is

significantly different for process B and process C. This suggests that d_{ss} is strongly dependent on other process conditions.

3.6.4 Pad Deformation Limit, d_{max}

Figure 3.8d shows the dependence of d_{max} on density and process. The parameter d_{max} is the height at which the pad just contacts the down area. Similar to d_{ss}, d_{max} is a measure of the rigidity of the polishing pad, except that it depends on the amount of oxide up area (instead of nitride up area) that is supporting the polishing pad. Hence, it has the same shape as Figure 3.8c but has the reverse dependence on density. As with the results for d_{ss}, processes A and B have similar d_{max}, and process C has the smallest d_{max}.

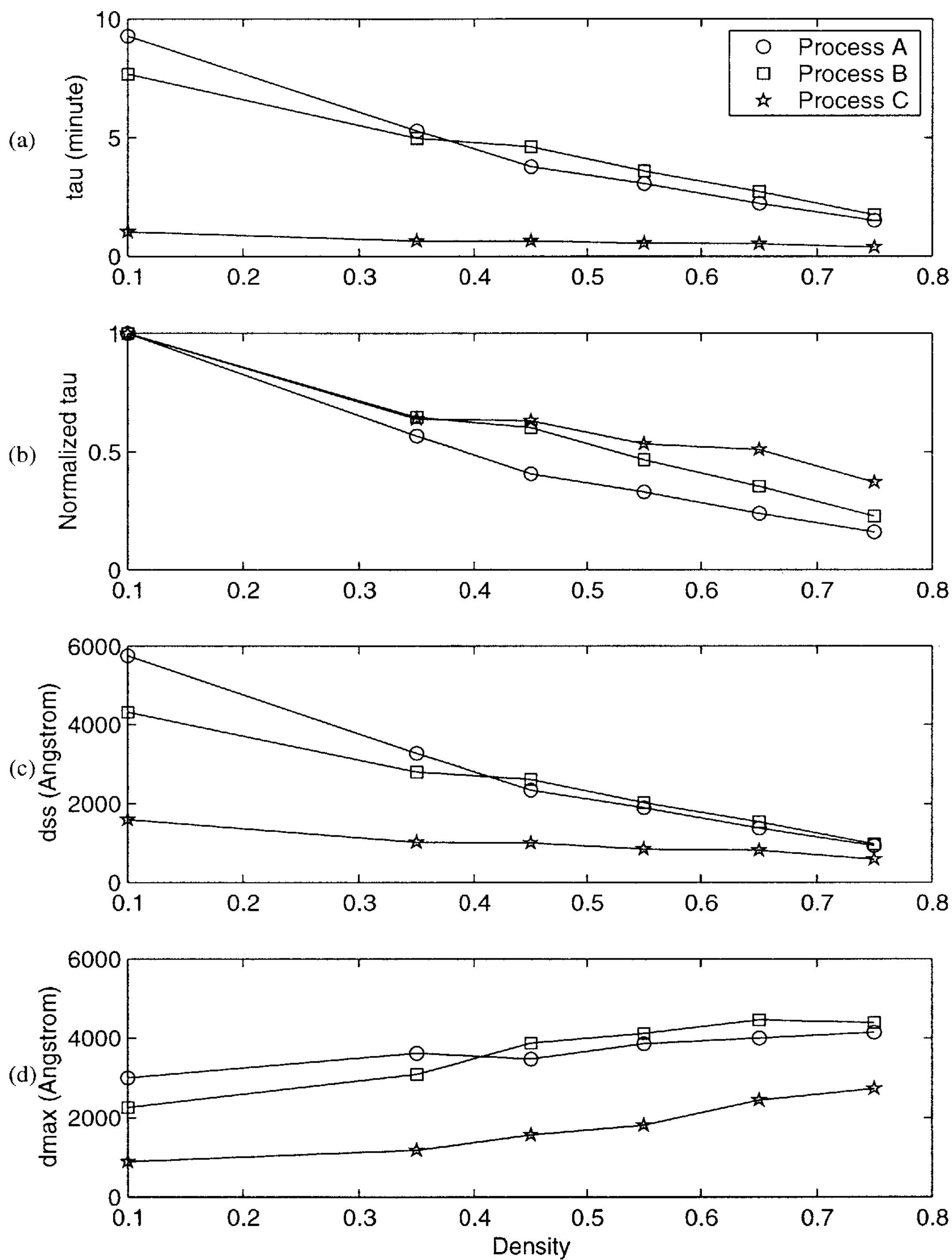

Figure 3.8 Dependence of model parameters on density: (a) τ, (b) normalized τ, (c) d_{ss}, (d) d_{max}.

3.7 Additional Modeling Results

In this section, several additional modeling results are discussed. The results shown here are theoretical calculations based on the CMP model described in Sections 3.2 and 3.3, and the values of the model parameters shown in Table 3.2. In this way, the effects of pattern density, initial step height, and slurry selectivity on post-CMP step height and nitride erosion uniformity can be studied. The results can serve as guidelines to optimize the CMP process before any actual polishing is done.

3.7.1 Pattern Density

Variations in pattern density cause uneven polishing within a die. The impact of this on polish uniformity is illustrated in Figure 3.9, which shows step height and nitride erosion as a function of polish time for each of the three processes A, B, and C. The step height and nitride erosion curves corresponding to the 10%, 35%, 45%, 55%, 65%, and 75% pattern density regions are shown.

The graphs show that initially, step height decreases most rapidly for the high pattern density regions and as polishing progresses, the step height levels off. This is because initially, the high features supporting most of the polishing pad are the oxide in the trenches. In the high pattern density regions, the oxide density is small, hence the oxide removal rate is high. This causes the local step height to decrease very rapidly. During overpolishing, the polishing pad is supported mostly by the nitride areas. In the high pattern density regions, the amount of pad deformation into the trenches is small. Hence, the step height rapidly converges to d_{ss}.

Another interesting observation is that the spread in local step height across regions with different densities increases initially, then decreases to a minimum, and finally increases again as shown. Hence, the model shows that there is an optimal polishing time at which the spread in step height is minimum regardless of density. Similar results are obtained for nitride erosion. This is intriguing because this shows that in order to obtain good within-die uniformity, some step height (dishing) and erosion must be permitted. Unfortunately, the model also shows that the polish time that minimizes the spread in step height is different from the polish time that minimizes the spread in nitride erosion. Hence, there is a compromise between step height and dishing uniformity. Recall from earlier in this chapter that step height is measured relative to the top of the nitride surface. Hence, variations in nitride erosion and step height sum together to give variations in the final oxide thickness in the trenches.

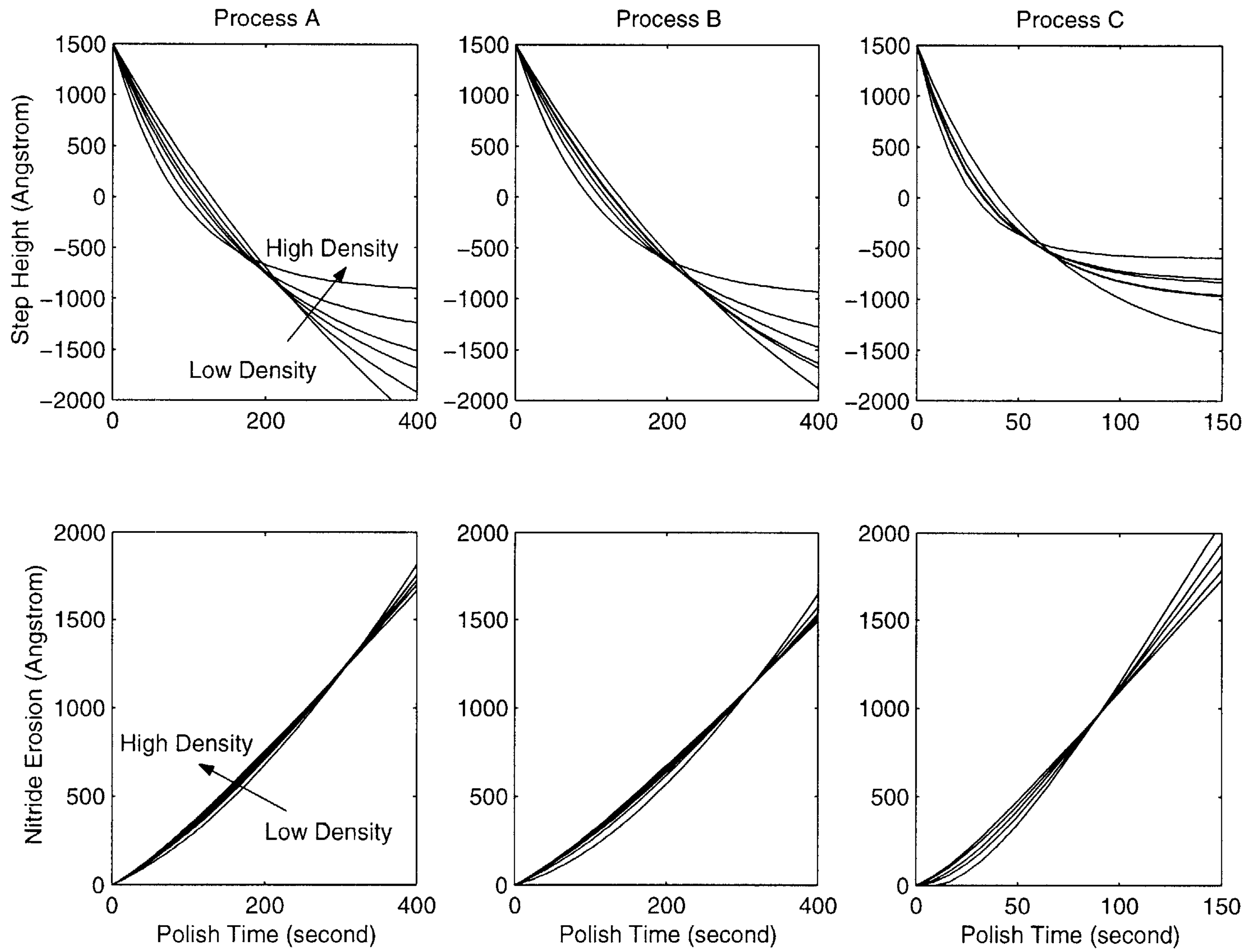

Figure 3.9 Time evolution of step height and nitride erosion for a range of pattern densities. (Note: The horizontal scale for process C is different).

3.7.2 Initial Step Height

Figure 3.10 shows how the pre-CMP step height affects the spread in step height, the step height at which spread is a minimum, and the polish time at which this minimum occurs. The step height curves are for process A, and are calculated using initial step heights of 1000 Å, 2000 Å, and 4000 Å. The corresponding graphs are shown in Figures 3.10a, 3.10b, and 3.10c respectively.

Several important results can be drawn from Figure 3.10. Firstly, increasing the initial step height decreases polish uniformity across different densities. This can be shown by comparing the largest vertical distance between the lowest density curve and the highest density curve before the minimum spread is reached. Figure 3.10 shows that the spread in step height in the initial polish phase is largest when the initial step height is 4000 Å, and smallest when the initial step height is 1000 Å. Alternatively, the difference in time at which the step height is zero for the lowest density curve and the highest density curve can be measured. The size of this "overpolish window" is a good indicator of how uniformly polishing occurs across different densities. The overpolish window is largest when the initial step height is 4000 Å as shown.

Secondly, increasing the initial step height increases the amount of dishing at which the spread in step height is minimum. The arrows in Figure 3.10 mark the points at which the spread in step height is minimum. The average amount of dishing "penalty" is about 600 Å for d_0 = 1000 Å, 750 Å for d_0 = 2000 Å, and 1000 Å for d_0 = 4000 Å. The spread in dishing at these points also increases with increasing initial step height.

Thirdly, the polish time when the spread in step height is minimum increases with increasing initial step height. The amount of polishing required to reach the minimum

spread in step height is about 150 s for $d_0 = 1000$ Å, 200 s for $d_0 = 2000$ Å, and 400 s for $d_0 = 4000$ Å.

Thus, the model shows that it is desirable to make the initial step height as small as possible. Having a small initial step height decreases the spread in step height and consequently the amount of overpolishing required. It also reduces the amount of dishing "penalty" in order to obtain uniformity across a range of densities. Finally, it reduces the polish time required to reach the minimum spread in step height.

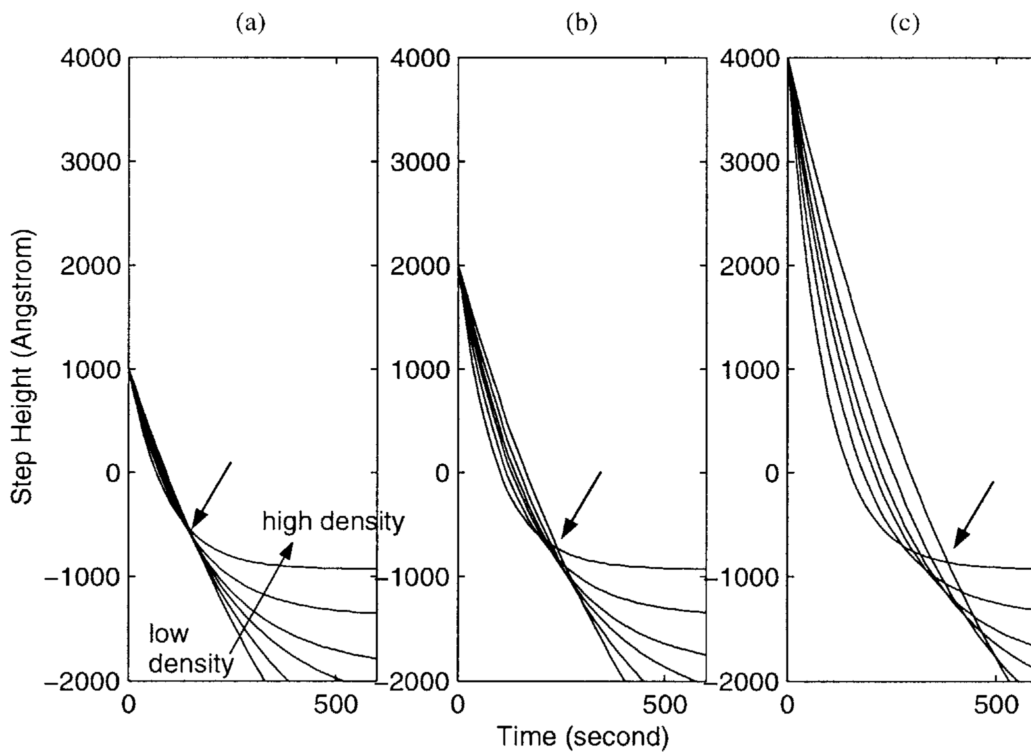

Figure 3.10 Effect of pre-CMP step height on post-CMP step height: (a) d_0 = 1000 Å, (b) d_0 = 2000 Å, (c) d_0 = 4000 Å.

3.7.3 Oxide to Nitride Selectivity

Standard silica-based slurries commonly used in STI CMP today have oxide to nitride selectivities that range from 2:1 to 5:1. To obtain high wafer throughput in manufacturing, the amount of time spent polishing each wafer is reduced by increasing the polish rate. As a result, the nitride removal rate is high, with values that range from a few hundred to more than a thousand angstroms per minute, depending on the process conditions used. The high nitride removal rate can cause significant nitride erosion to occur, especially during overpolishing. This may in turn damage the silicon active area underneath the nitride. Hence, high selectivity slurries are of great interest. In fact, slurries with greater than 200:1 selectivity have been developed [25]. High selectivity to nitride can be obtained by dramatically reducing the nitride removal rate to tens of angstroms per minute while maintaining a high oxide removal rate.

Figure 3.11 shows the effect of selectivity on polish uniformity. The step height and nitride erosion curves for process A are shown. Figure 3.11a is plotted using the values of K_{ox} and K_{nit} in Table 3.2 (selectivity = 3.72:1). Figure 3.11b is plotted using the same K_{ox} but $K_{nit} = 0.01 \times K_{ox}$ (selectivity = 100:1).

Comparing the step height plots shows that increasing the oxide to nitride selectivity improves polish uniformity by reducing the spread in step height and the size of the overpolish window, and the polish time needed to reach the minimum spread in step height. However, it increases the dishing "penalty". The steady state dishing also increases as expected since from equation (3.13):

$$d_{ss} = \tau \left(K_{ox} - K_{nit} \right) \tag{3.13}$$

Comparing the nitride erosion plots shows that nitride erosion is reduced dramatically as expected. Notice that the vertical scale for nitride erosion in Figure 3.11b is larger.

In conclusion, the model predicts that using high selectivity slurries does improve CMP performance by reducing the polish non-uniformity due to pattern density effects and by reducing the amount of nitride erosion. However, excessive overpolishing can result in more dishing than if lower selectivity slurry is used.

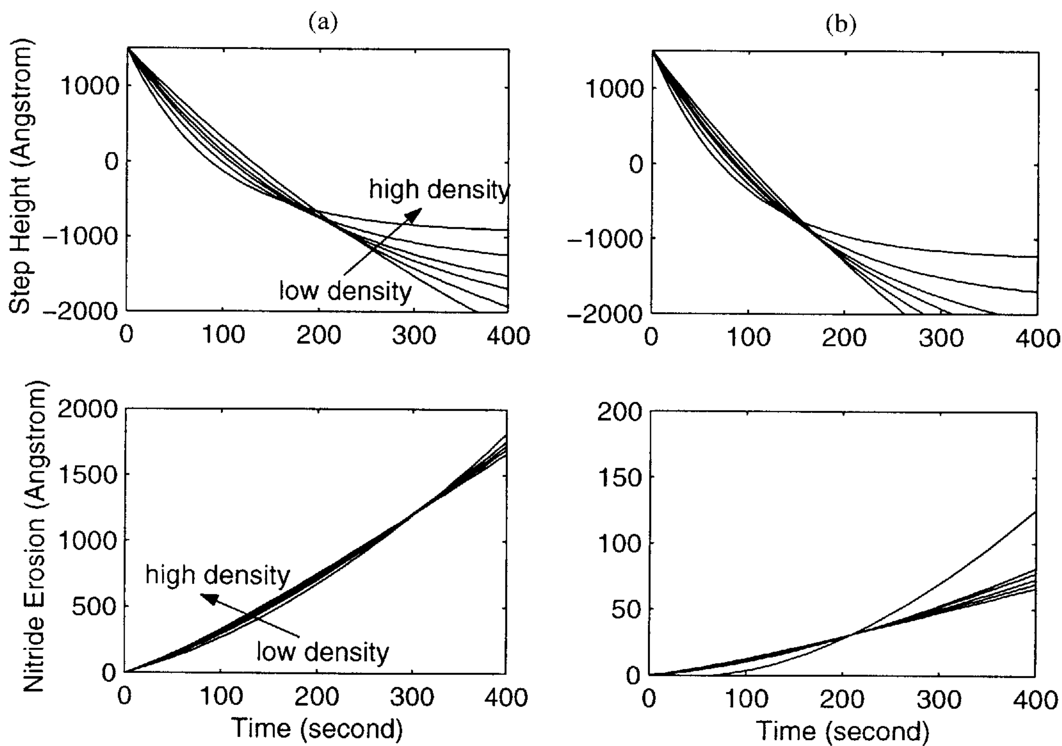

Figure 3.11 Effect of high selectivity slurry on step height and nitride erosion: (a) standard silica based slurry with 3.7:1 selectivity, (b) 100:1 selectivity slurry. Notice the larger scale for nitride erosion.

Chapter 4
Combined Planarization Length Parameter Extraction Methodology

In this chapter, a refinement to the parameter extraction methodology is presented. The method described in the previous chapter used the designed pattern densities in its calculations. However, we know from experience that the surface of a post-CMP die is continuously varying and abrupt steps corresponding to abrupt changes in final oxide thickness due to pattern density variations are not observed. We can infer from this that during polishing, some averaging of the surrounding densities occurs, and this density effect has been shown to be the primary effect in oxide inter-level dielectric polishing [13]. Thus, we consider here an improvement in the extraction method by using the effective density at each measurement point instead of the designed pattern density.

A method for calculating the average density due to CMP was described by Ouma [21]. The updated extraction methodology described here integrates the average density calculation with the basic extraction method described in Chapter 3. Section 4.1 briefly reviews the concept of planarization length and how it can be used to calculate the average density. Section 4.2 describes the updated parameter extraction methodology, and the results are shown in Section 4.3.

4.1 Density Averaging using Planarization Length

CMP achieves planarization in two ways: (1) it removes topography by selectively removing material from the up areas faster than the down areas; and (2) it reduces step height variations by averaging the local density. Step height removal was discussed using the removal rate-step height model in the previous chapter. In the following discussion, we look at how we can model density averaging.

According to Ouma, the average density of any point on a wafer can be calculated by taking the weighted average of the pattern densities inside a window centered at that point [21]. The window size is determined by a single parameter known as the planarization length. Physically, planarization length defines the length scale over which planarity is achieved. This length scale is easily visualized by polishing a step density pattern. As shown in Figure 4.1, away from the density boundary, uniform polishing occurs at a removal rate given by the MIT density model. The oxide in the patterned region polishes faster than the oxide in the unpatterned region. This introduces a step height in the regions that are far away from the boundary. Close to the boundary, the oxide thickness changes gradually from the patterned region to the unpatterned region. The length of this transition region represents the planarization length.

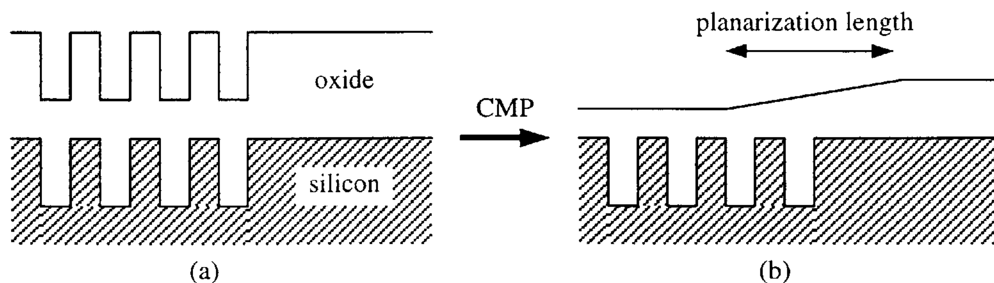

Figure 4.1 Physical meaning of planarization length: (a) cross-section before CMP, (b) cross-section after CMP, showing the transition region near the step density boundary.

Once the planarization length is known, the effective density at any point on a layout can be calculated. A weighting function is used to calculate the effective density inside the averaging window. The optimal weighting function is an elliptic weighting filter and it is shaped like the deformation profile of a polishing pad [21]. Figure 4.2 shows the effective density maps of the STI CMP characterization mask for different planarization lengths. Figure 4.2a shows the top view of the die as it is patterned on the wafers. Figures 4.2b and 4.2c show the effective density contour maps for planarization lengths of 3.2 mm and 5.2 mm respectively. Clearly, a longer planarization length is more effective at smoothing topography.

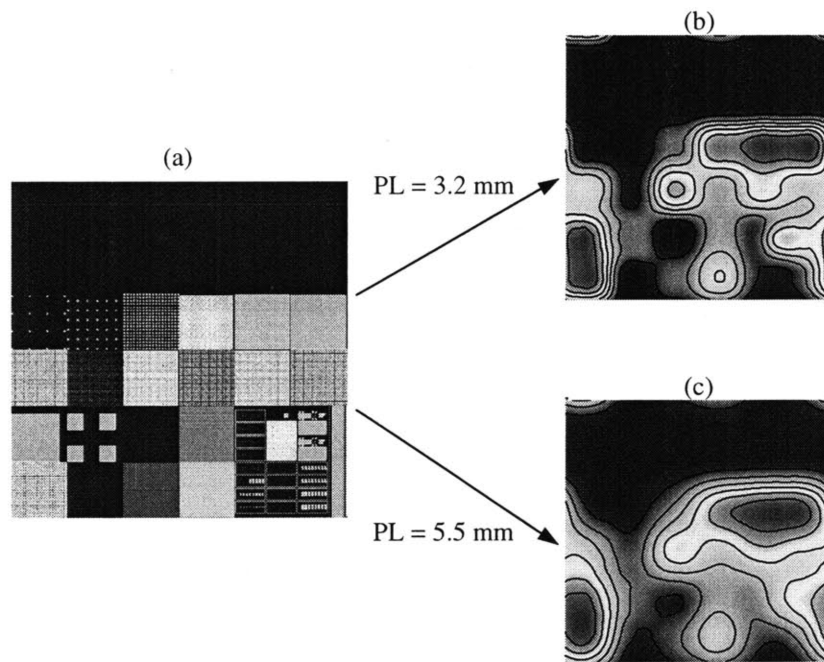

Figure 4.2 Density averaging: (a) layout of STI CMP characterization mask; (b) density map using 3.2 mm planarization length; (c) density map using 5.5 mm planarization length.

Another way of visualizing how having a longer planarization length reduces topography is to see how the distribution of effective density changes with planarization length. Figure 4.3 shows the distribution of effective density on the STI CMP characterization mask for three different planarization lengths. Figures 4.3a, 4.3b, and 4.3c show the histogram for planarization lengths of 3 mm, 5 mm, and 7 mm respectively. The histograms show that increasing the planarization length reduces the spread of effective densities and distributes the densities more evenly. These help to improve polish uniformity as discussed in Chapter 3.

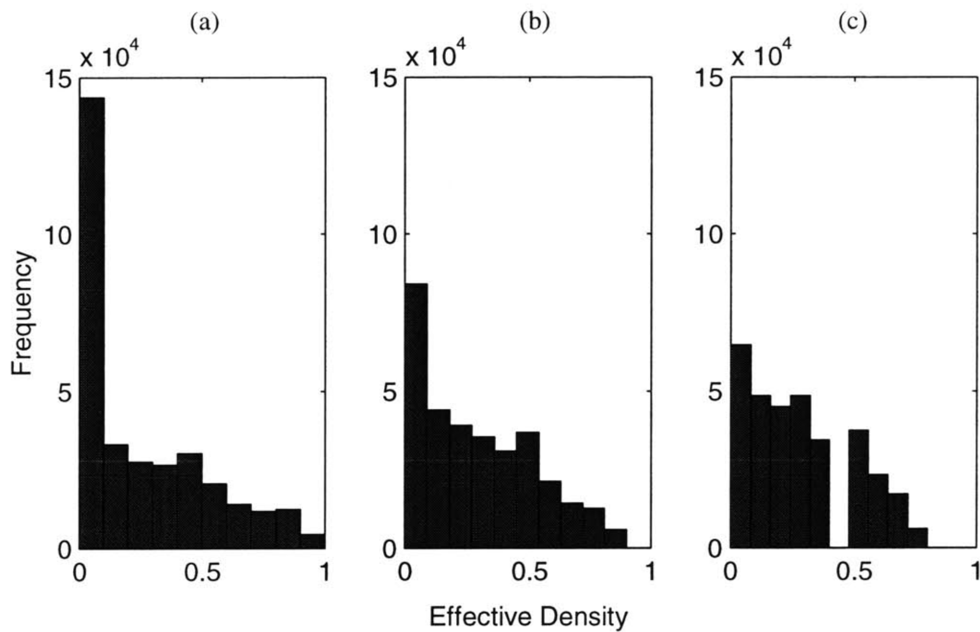

Figure 4.3 Effective density distribution for planarization lengths of: (a) 3 mm, (b) 5 mm, (c) 7 mm.

4.2 Improved Parameter Extraction Methodology

The improved parameter extraction methodology can be considered to be a generalization of the basic method described in the previous chapter. If the planarization length is chosen to be less than the length of each cell (3.5 mm) in the step density region, the effective density ρ_i as measured from the center of each cell will be approximately the designed pattern density and the results from the parameter extraction will be the same as the results obtained in Table 3.2. Hence, the improved methodology allows processes of any planarization length to be modeled.

Density averaging is done by convolving the averaging window and the layout. To do this, the 21.095 mm $\times$ 21.095 mm layout is first discretized into 37 µm cells using SiCat™. The output is a 570 $\times$ 570 matrix (21.090 mm $\times$ 21.090 mm effective size), where each element in the matrix represents the average density in a corresponding 37 µm $\times$ 37 µm area on the layout. In those locations where the length of the active area is less than or equal to 1 µm, the corresponding location in the matrix is replaced with zeros. This is because HDP oxide deposition is used during fabrication, which planarizes these small features. In addition, reverse tone etch back is not performed on these features, so the exposed nitride density is effectively zero.

Since the planarization lengths for processes A, B, and C are not known *a priori*, they are chosen by optimizing the total sum-squared error given by a variant of equation (3.16) for each process:

$$\underset{PL,\, K_{ox},\, K_{nit},\, \tau_i}{\arg\min} \sum_{j=1}^{J} \sum_{i=1}^{I} \left\{ \left[H_i(t_j) - h_i(t_j) \right]^2 + \left[E_i(t_j) - e_i(t_j) \right]^2 \right\} \tag{4.1}$$

The optimization process is shown graphically in Figure 4.4. First, an arbitrary value for planarization length (*PL*) is chosen. The planarization length determines the size of the averaging window of the averaging function. An elliptical averaging function is then used to calculate the effective density of the die (as seen by the polishing pad) by convolving the elliptical function with the discretized die layout. The effective density for each measurement site can then be found. Finally, using the measurements and the effective densities, a multivariate optimization is performed to find K_{ox}, K_{nit}, and τ as per the basic parameter extraction methodology. This process is repeated until the planarization length that minimizes equation (4.1) is found.

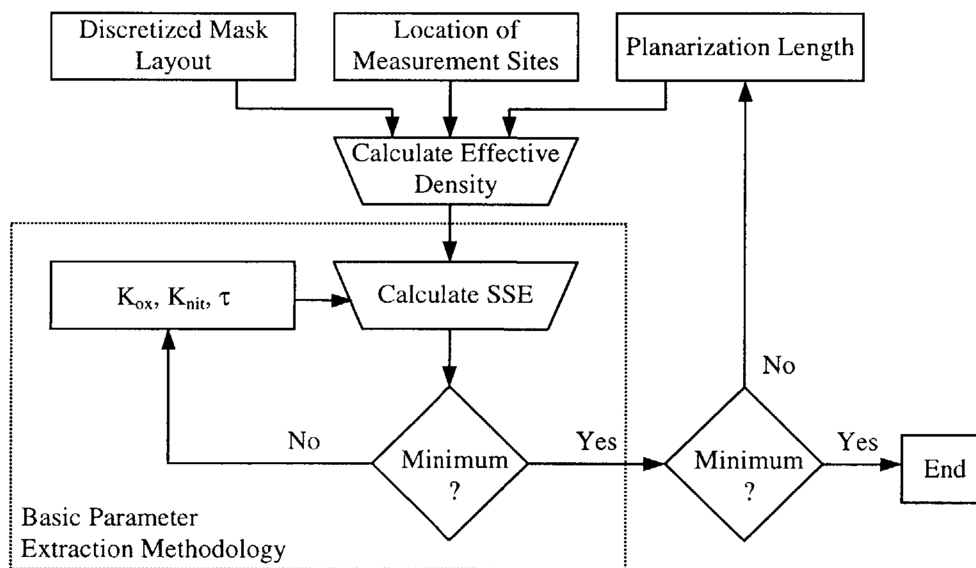

Figure 4.4 Flow chart of updated parameter extraction methodology

4.3 Results and Discussion

The improved parameter extraction methodology achieves an improvement in fit as shown in Table 4.1. Table 4.1 lists the RMS errors for step height and nitride erosion for each process and pattern density. It also lists the total RMS error for each process, which is defined as:

$$Total\ RMS\ Error = \sqrt{\frac{SSE}{i \times j}} \tag{4.2}$$

The total RMS error is a simple measure of the overall fit error. The change in error from Table 3.3 is shown in parentheses. Finally, Figure 4.5 shows the corresponding effective density for each pattern density on the die.

Table 4.1 shows that the total RMS error is reduced for processes B and C, but it is unchanged for process A. The values are unchanged for process A because it has a planarization length of 3.2 mm, which is shorter than the length of each cell in the step density region. As mentioned earlier, this means that the effective density at the measurement sites are the same as the designed pattern density. Hence, the results from the parameter extraction are the same as expected. On the other hand, the planarization length for processes B and C is 5.5 mm. The results show that using the effective density to extract the model parameters produces a better fit. Although the RMS error for certain densities are larger, the maximum RMS error and the total RMS error are smaller.

The improved parameter extraction methodology achieves a 5.5% and 2.9% reduction of the total RMS error for processes B and C by fitting an additional parameter,

the planarization length. What is significant about the improved methodology is that it adds realism to the model by using planarization length to compute effective density. The fact that this improves the accuracy of the fit suggests that the proposed reverse tone etch back STI CMP model captures the correct dependencies.

Table 4.1 RMS errors using the updated parameter extraction methodology. Changes from Table 3.3 are shown in parentheses.

	Process A		**Process B**		**Process C**	
Planarization Length (mm)	3.2		5.5		5.5	
Total RMS Error (Å)	39.7 (0)		49.4 (-2.9)		66.4 (-2.0)	
Pattern Density (%)	**Step Height RMS Error (Å)**	**Nitride Erosion RMS Error (Å)**	**Step Height RMS Error (Å)**	**Nitride Erosion RMS Error (Å)**	**Step Height RMS Error (Å)**	**Nitride Erosion RMS Error (Å)**
10	43.5 (0)	65.3 (0)	49.5 (-2.8)	80.2 (-11.6)	112.8 (-3.0)	100.6 (-29.5)
35	24.4 (0)	32.8 (0)	48.7 (+4.8)	41.6 (-1.6)	18.1 (-1.3)	40.8 (-16.3)
45	25.0 (0)	37.2 (0)	36.7 (+1.9)	54.1 (+6.5)	54.8 (+1.9)	40.5 (-7.6)
55	24.0 (0)	37.3 (0)	42.2 (-2.6)	35.2 (-6.0)	27.1 (+3.3)	73.1 (+11.9)
65	18.2 (0)	43.4 (0)	28.1 (-3.5)	40.8 (-7.6)	46.8 (+2.0)	64.9 (+4.3)
75	51.6 (0)	47.4 (0)	64.8 (-3.9)	48.0 (-2.6)	21.6 (+4.2)	102.4 (+20.3)

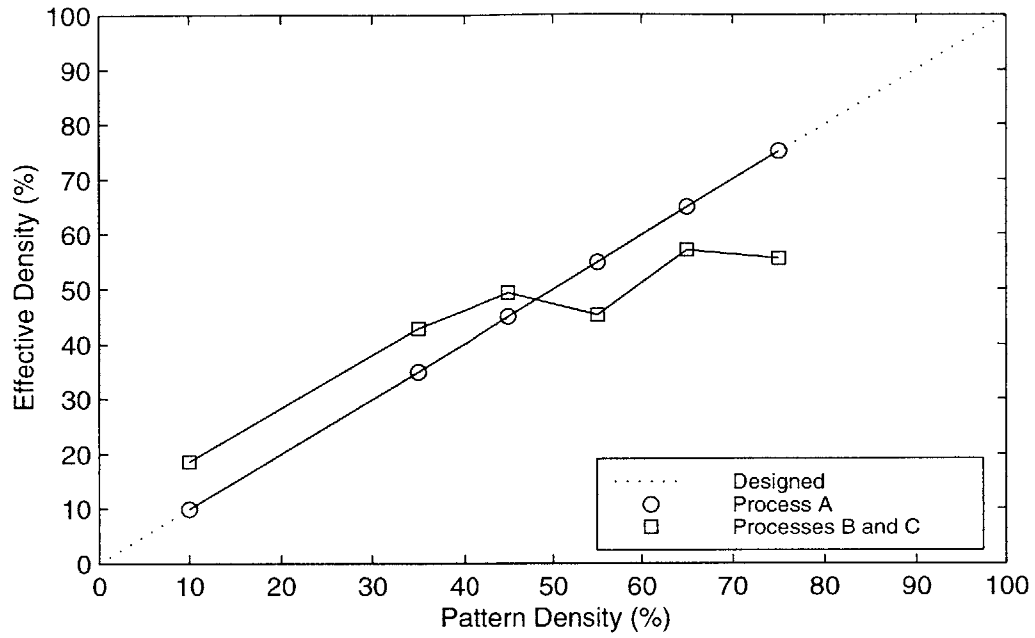

	Density (%)					
Designed	10.0	35.0	45.0	55.0	65.0	75.0
Process A (PL = 3.2 mm)	9.9	35.0	45.1	54.9	65.0	75.1
Process B, C (PL = 5.5 mm)	18.6	42.9	49.2	45.4	57.1	55.6

Figure 4.5 Effective density vs. pattern density

Chapter 5
Conclusion and Future Work

This work has examined chemical mechanical polishing for shallow trench isolation, in particular, shallow trench isolation fabrication using the reverse tone etch back technique. The main contribution of this work is reverse tone etch back STI CMP modeling, beginning with an introduction to device isolation in Chapter 1, which provided motivation for device isolation, and presented two common isolation techniques: LOCOS and STI. Chapter 2 introduced CMP as an enabling technique for STI formation, highlighted some of the problems encountered during STI CMP, and presented the reverse tone etch back technique as a solution to some of these problems. A removal rate vs. step height model for reverse tone etch back STI CMP was developed in Chapter 3, and further extended to incorporate density averaging effects in Chapter 4. This chapter concludes this work with a summary of the main results from this study and a presentation of some model applications. Areas for future work are also identified.

5.1 STI CMP Modeling

A reverse tone etch back STI CMP model incorporating density averaging effects was developed and validated using experimental data. The model confirms that die-level density variations cause polish non-uniformity. Hence, more uniform polishing can be achieved by using processes with longer planarization lengths to reduce the effective density spread. Polish uniformity can be further improved by reducing the pre-CMP step

height and by using slurries with high oxide to nitride selectivity. Furthermore, the model predicts that the density effects on polish uniformity can be almost completely eliminated by slightly overpolishing the wafers. Although some dishing occurs as a result of overpolishing, almost constant dishing across a range of densities can be achieved. The contribution of nitride erosion variations to post-CMP non-uniformity is small, especially when high selectivity slurries are used. In addition, it was shown that having a smaller initial step height also improves polish uniformity.

5.2 Applications of the Methodology

Accurate film thickness prediction during CMP is useful for many applications. The results from the modeling can be used for process improvement and optimization. One such application is to determine the optimal film thickness that must be deposited for any given planarization requirement. The model can also be used to rapidly characterize existing and new processes. These results can be used to predict the optimum process conditions. This reduces the amount of guess work needed to optimize the CMP process, which shortens process development time and reduces consumable waste. These time and cost savings can be substantial for a typical manufacturing plant.

5.3 Future Work

A method for characterizing CMP processes using the STI CMP characterization mask was described and demonstrated. Total RMS errors of less than 100 Å were obtained. However, additional work is still needed to further validate the model and answer some unexpected results.

5.3.1 Validation on Non-Standard Structures

The STI structures that are used for this study are square patterns with 80μm pitch which are meant to emulate isolated active areas. The current model says that for any given process, the post-CMP step height and nitride erosion depends only on the initial step height, and the effective density. Future experiments should investigate if the shape and size of the active area affects step height and erosion. A more comprehensive characterization mask might include active areas of different shapes and sizes, as well as structures with constant density/varying pitch and constant pitch/varying density. In addition, the model was applied to relatively large active areas and trench (smallest active area length = 25.3 μm); further work is needed to measure, analyze, and potentially extend the model for very small features where polish may be accelerated.

5.3.2 Process Variations

The results for wafers with different starting step heights and processes using high selectivity slurries were predicted using the proposed model and the extracted model parameters. These predictions should be verified in future experiments.

5.3.3 Steady-State Dishing (d_{ss}) and Pad Deformation Limit (d_{max})

Some guess work can be eliminated from the model by running controlled experiments to experimentally determine d_{ss} or d_{max}. For example, d_{ss} can be found by severely overpolishing STI wafers with a thick (>1µm) nitride layer until steady-state dishing is achieved. Likewise, d_{max} can be found by carefully polishing of STI wafers with large (> 5000 Å) initial step heights in small time increments.

5.3.4 K_{ox} and K_{nit}

The extracted values for K_{ox} and K_{nit} are smaller than the removal rates obtained by polishing blanket oxide and nitride wafers respectively. In addition, the oxide to nitride selectivity obtained using the parameter extraction methodology is higher than expected. Some additional modeling work is needed to explain these differences in results.

Table 5.1 Expected and extracted values for K_{ox}, K_{nit}, and selectivity

	Process A	Process B	Process C
Blanket Oxide RR (Å/min)	1031	938	2179
K_{ox} (Å/min)	848	771	2189
Blanket Nitride RR (Å/min)	—	—	783
K_{nit} (Å/min)	228	207	628
Measured Selectivity	2.44 [1]	2.44 [2]	2.78
Extracted Selectivity	3.72	3.72	3.49

[1] value obtained from previous characterization experiments

[2] estimated value, assuming the effect of pad type on selectivity is small

Bibliography

[1] M. Nandakumar, A. Chatterjee, S. Sridhar, K. Joyner, M. Rodder, and I.-C. Chen, "Shallow Trench Isolation for Advanced ULSI CMOS Technologies," *International Electron Devices Meeting, IEDM '98 Technical Digest*, pp. 133-136, 1998.

[2] A. Chatterjee, J. Esquivel, S. Nag, I. Ali, D. Rogers, K. Taylor, K. Joyner, M. Mason, D. Mercer, A. Amerasekera, T. Houston, and I.-C. Chen, "A Shallow Trench Isolation Study for 0.25/0.18um CMOS Technologies and Beyond," *1996 Symposium on VLSI Technology, Digest of Technical Papers*, pp. 156-157, 1996.

[3] Andres Bryant, Wilfried Hänsch, and Toshio Mii, "Characteristics of CMOS Device Isolation for the ULSI Age," *International Electron Devices Meeting, Technical Digest*, pp. 671-674, 1994.

[4] International Technology Roadmap for Semiconductors, 1999.

[5] S. M. Sze, *VLSI Technology*, McGraw-Hill, 1988.

[6] J. Song, "Process Capability of Local Oxidation of Silicon Isolation Technology for Sub-Half Micrometre Custom IC Applications," *Electronics Letters*, Vol. 35, No. 6, pp. 505-506, 18 March 1999.

[7] Stephen A. Campbell, *The Science and Engineering of Microelectronic Fabrication*, Oxford University Press, 1996.

[8] C. Y. Chang, S. M. Sze, *ULSI Technology*, McGraw-Hill, 1996.

[9] John O. Borland and H. T. Cho, "LOCOS-vs.-Shallow Trench Isolation Latch-up Using MeV Implantation for Well Formation Down to 0.18um Design Rules," *1998 International Conference on Ion Implantation Technology Proceedings*, Vol. 1, pp. 67-70, 1999.

[10] Pierre C. Fazan and Viju K. Mathews, "A Highly Manufacturable Trench Isolation Process for Deep Submicron DRAMs," *International Electron Devices Meeting, Technical Digest*, pp. 57-60, 1993.

[11] Hung-Wen Chiou and Lai-Juh Chen, "One Step Effective Planarization of Shallow Trench Isolation," *Proceedings of the IEEE 1998 International Interconnect Technology Conference*, pp. 199-201, 1998.

[12] N. Elbel, Z. Gabric, W. Langheinrich, and B. Neureither, "A New STI Process Based on Selective Oxide Deposition," *1998 Symposium on VLSI Technology, Digest of Technical Papers*, pp. 208-209, 1998.

[13] B. E. Stine, D. O. Ouma, R. R. Divecha, D. S. Boning, J. E. Chung, D. L. Hetherington, C. R. Harwood, O. S. Nakagawa, and S.-Y. Oh, "Rapid Characterization and Modeling of Pattern-Dependent Variation in Chemical-Mechanical Polishing," *IEEE Transactions on Semiconductor Manufacturing*, Vol. 11, No. 1, pp. 129-140, February 1998.

[14] B. Davari, C. W. Koburger, R. Schulz, J. D. Warnock, T. Furukawa, M. Jost, Y. Taur, W. G. Scheittek, J. K. DeBrosse, M. L. Kerbaugh, and J. L. Mauer, "A New Planarization Technique, Using a Combination of RIE and Chemical Mechanical Polishing (CMP)," *International Electron Devices Meeting, Technical Digest*, pp. 61-64, 1989.

[15] Y. Wu, J. Gilhooly, and B. Philips, "Control Methods for the Chemical-Mechanical Polishing Process in Shallow Trench Isolation," *1998 IEEE/SEMI Advanced Semiconductor Manufacturing Conference & Workshop*, pp. 66-70, 1998.

[16] T. Tugbawa, T. Park, D. Boning, T. Pan, P. Li, S. Hymes, T. Brown, and L. Camilletti, "A Mathematical Model of Pattern Dependencies in Cu CMP Processes," *CMP Symposium, Electrochemical Society Meeting*, Honolulu, HA, October 1999.

[17] B. Lee, D. S. Boning, D. L. Hetherington, and D. J. Stein, "Using Smart Dummy Fill and Selective Reverse Etchback for Pattern Density Equalization," *Chemical Mechanical Polish for ULSI Multilevel Interconnection Conference (CMP-MIC)*, pp. 255-258, Santa Clara, March 2000.

[18] E. P. Giannelis and Y. Y. Shacham-Diamand, "Spin-On Films Add New Dimension to ULSI Circuits," *IEEE Circuits and Devices Magazine*, Vol. 9, No. 6, pp. 30-34, November 1993.

[19] B. Stine, D. Ouma, R. Divecha, D. Boning, J. Chung, D. L. Hetherington, I. Ali, G. Shinn, J. Clark, O. S. Nakagawa, and S.-Y. Oh, "A Closed-Form Analytic Model for ILD Thickness Variation in CMP Processes," *1997 Chemical Mechanical Polish for ULSI Multilevel Interconnection Conference (CMP-MIC)*, pp. 266, Santa Clara, February 1997.

[20] T. H. Smith, S. J. Fang, D. S. Boning, G. B. Shinn, and J. A. Stefani, "A CMP Model Combining Density and Time Dependencies," *1999 Chemical Mechanical Polish for ULSI Multilevel Interconnection Conference (CMP-MIC)*, Santa Clara, February 1999.

[21] Dennis Okumu Ouma, "Modeling of Chemical Mechanical Polishing for Dielectric Planarization," Ph.D. Thesis, Massachusetts Institute of Technology, 1998.

[22] J. Grillaert, M. Meuris, N. Heyley, K. Devriendt, E. Vrancken, and M. Heyns, "Modeling Step Height Reduction and Local Removal Rates Based on Pad-Substrate Interactions," *1998 Chemical Mechanical Polish for ULSI Multilevel Interconnection Conference (CMP-MIC)*, pp.79-86, Santa Clara, February 1998.

[23] Peter A. Burke, "Semi-Empirical Modeling of SiO2 Chemical-Mechanical Polishing Planarization," *1991 VMIC Conference*, pp. 379-384, June 11-12 1991.

[24] E. Tseng, C. Yi, and H. C. Chen, "A Mechanical Model for DRAM Dielectric Chemical-Mechanical Polishing Process," *1997 Chemical Mechanical Polish for ULSI Multilevel Interconnection Conference (CMP-MIC)*, pp. 258-265, Santa Clara, February 1997.

[25] S. D. Hosali, A. R. Sethuraman, J.-F. Wang, L. M. Cook, and D. R. Evans, "Planarization Process and Consumable Development for Shallow Trench Isolation," *1997 Chemical Mechanical Polish for ULSI Multilevel Interconnection Conference (CMP-MIC)*, pp. 52-57, Santa Clara, February 1997.

Appendix A-1
Planarization Length Optimization for Process A

```
% Created March 29, 2000. Terence Gan.
% Run this to optimize PL and parameters for process A.

x = [4000];      % initial estimate for planarization length

options             = optimset('fminsearch');
options.TolFun      = 1;
options.TolX        = 1;
options.MaxFunEvals = 100000;
options.MaxIter     = 100000;

xOpt = fminsearch('pla_exe2', x,options,dmask,pl_xy,37);

% variable declarations --------------------------------

global den       % effective density
global Kox       % oxide removal rate
global Knit      % nitride removal rate
global total_rms % total RMS error
global tau       % exponential time constant
global dss       % steady state dishing
global Hrms      % step height rms errors
global Erms      % nitride erosion rms errors

% display summary of results ---------------------------

pl = xOpt
Kox
Knit
total_rms
den
tau
dss
dmax = tau.*((1-den)*Knit+den*Kox)./(1-den)
Hrms
Erms
```

Appendix A-2
Density and Parameter Extraction for Process A

```
function [cost] = pla_exe2(pl,dmask,pl_xy,cell_length)

% Created March 29, 2000. Terence Gan.
% This is the first inner optimization loop, it is the
% cost function for optimizing the planarization length.
% It uses the input planarization length to extract the
% effective density at each of the measurement points.

% pl          = planarization length (um)
% dmask       = discretized mask layout
% pl_xy       = xy-coordinates of measurement points (um)
% cell_length = level of discretization in dmask (um)

% get effective density

global den
den = pl_get_density(dmask,pl_xy,pl,cell_length);

% minimize sum-squared error between model and data
% using another optimization loop

x                   = [800 200 5 5 5 5 5 5];
options             = optimset('fminsearch');
options.TolFun      = 1e-3;
options.TolX        = 1e-3;
options.MaxFunEvals = 100000;
options.MaxIter     = 100000;
xOpt                = fminsearch('pla_exe3', x,options,den);

% display planarization length with each iteration

pl

% display total_rms with each iteration

global total_rms
total_rms

% use the same cost from the plb_exe3 loop

global cost
```

Appendix A-3
Cost Function for Process A

```
function [cost] = pla_exe3(x,den)

% Created March 29, 2000. Terence Gan.
% This is the second inner optimization loop, it is the
% cost function for optimizing Kox, Knit, and tau by
% minimizing the sum-squared error between the model and
% the measurement data.

% x   = vector containing Kox, Knit, and tau
% den = vector of effective density

% step height measurements

h10 = [ 319  104 -155 -337 -781  -980 -1087];
h35 = [ 192   13 -217 -423 -810 -1003 -1070];
h45 = [ 117  -70 -287 -480 -835 -1005 -1061];
h55 = [  81 -141 -280 -481 -797  -922 -1005];
h65 = [ -32 -206 -364 -526 -771  -892  -934];
h75 = [-104 -210 -348 -451 -649  -732  -779];

% nitride erosion measurements

e10 = [ 283  314  426  479  757  942 1013];
e35 = [ 339  365  464  528  748  881  916];
e45 = [ 342  377  466  525  737  859  904];
e55 = [ 353  398  488  547  758  868  922];
e65 = [ 354  396  491  563  755  859  897];
e75 = [ 368  406  509  564  756  875  913];

% initial step height measurements (pre-CMP)

d10 = [1313 1596 1292 1629 1437 1414 1690];
d35 = [1313 1595 1292 1630 1438 1415 1690];
d45 = [1321 1597 1298 1633 1446 1424 1697];
d55 = [1312 1597 1291 1629 1436 1413 1692];
d65 = [1321 1597 1297 1631 1445 1423 1695];
d75 = [1314 1595 1293 1629 1439 1415 1689];

% polish time

t   = [  90  124  127  168  211  230  253];

% variable declaration

global cost
global Kox
global Knit
global total_rms
global tau
global dss
global Hrms
```

```
global Erms

Kox    = x(1);
Knit   = x(2);

tau(1) = x(3);
tau(2) = x(4);
tau(3) = x(5);
tau(4) = x(6);
tau(5) = x(7);
tau(6) = x(8);

% calculating step height and nitride erosion using the model

dss = (Kox-Knit)*tau;

for i = 1:length(t),

  H10(i) = -(dss(1)+d10(i))*(1-exp(-t(i)/60/tau(1)))+d10(i);
  E10(i) = (Kox*Knit*t(i)/60 - ...
          Knit*(1-den(1))*(dss(1)+d10(i))*(1-exp(-t(i)/60/tau(1))))/...
         ((1-den(1))*Knit+den(1)*Kox);

  H35(i) = -(dss(2)+d35(i))*(1-exp(-t(i)/60/tau(2)))+d35(i);
  E35(i) = (Kox*Knit*t(i)/60 - ...
          Knit*(1-den(2))*(dss(2)+d35(i))*(1-exp(-t(i)/60/tau(2))))/...
         ((1-den(2))*Knit+den(2)*Kox);

  H45(i) = -(dss(3)+d45(i))*(1-exp(-t(i)/60/tau(3)))+d45(i);
  E45(i) = (Kox*Knit*t(i)/60 - ...
          Knit*(1-den(3))*(dss(3)+d45(i))*(1-exp(-t(i)/60/tau(3))))/...
         ((1-den(3))*Knit+den(3)*Kox);

  H55(i) = -(dss(4)+d55(i))*(1-exp(-t(i)/60/tau(4)))+d55(i);
  E55(i) = (Kox*Knit*t(i)/60 - ...
          Knit*(1-den(4))*(dss(4)+d55(i))*(1-exp(-t(i)/60/tau(4))))/...
         ((1-den(4))*Knit+den(4)*Kox);

  H65(i) = -(dss(5)+d65(i))*(1-exp(-t(i)/60/tau(5)))+d65(i);
  E65(i) = (Kox*Knit*t(i)/60 - ...
          Knit*(1-den(5))*(dss(5)+d65(i))*(1-exp(-t(i)/60/tau(5))))/...
         ((1-den(5))*Knit+den(5)*Kox);

  H75(i) = -(dss(6)+d75(i))*(1-exp(-t(i)/60/tau(6)))+d75(i);
  E75(i) = (Kox*Knit*t(i)/60 - ...
          Knit*(1-den(6))*(dss(6)+d75(i))*(1-exp(-t(i)/60/tau(6))))/...
         ((1-den(6))*Knit+den(6)*Kox);

end

% This calculates the sum-squared errors
% fminsearch tries to minimize the cost

Herr10 = H10-h10;
Herr35 = H35-h35;
Herr45 = H45-h45;
Herr55 = H55-h55;
```

```
Herr65 = H65-h65;
Herr75 = H75-h75;

Eerr10 = E10-e10;
Eerr35 = E35-e35;
Eerr45 = E45-e45;
Eerr55 = E55-e55;
Eerr65 = E65-e65;
Eerr75 = E75-e75;

error = [Herr10 Herr35 Herr45 Herr55 Herr65 Herr75 ...
       Eerr10 Eerr35 Eerr45 Eerr55 Eerr65 Eerr75 ];
cost = error*error';
total_rms = sqrt(cost/length(error));

Hrms10 = sqrt(Herr10*Herr10'/length(Herr10));
Hrms35 = sqrt(Herr35*Herr35'/length(Herr35));
Hrms45 = sqrt(Herr45*Herr45'/length(Herr45));
Hrms55 = sqrt(Herr55*Herr55'/length(Herr55));
Hrms65 = sqrt(Herr65*Herr65'/length(Herr65));
Hrms75 = sqrt(Herr75*Herr75'/length(Herr75));

Erms10 = sqrt(Eerr10*Eerr10'/length(Eerr10));
Erms35 = sqrt(Eerr35*Eerr35'/length(Eerr35));
Erms45 = sqrt(Eerr45*Eerr45'/length(Eerr45));
Erms55 = sqrt(Eerr55*Eerr55'/length(Eerr55));
Erms65 = sqrt(Eerr65*Eerr65'/length(Eerr65));
Erms75 = sqrt(Eerr75*Eerr75'/length(Eerr75));

Hrms = [Hrms10 Hrms35 Hrms45 Hrms55 Hrms65 Hrms75];
Erms = [Erms10 Erms35 Erms45 Erms55 Erms65 Erms75];
```

Appendix B-1
Planarization Length Optimization for Process B

```
% Created March 29, 2000. Terence Gan.
% Run this to optimize PL and parameters for process B.

x = [4000];       % initial estimate for planarization length

options             = optimset('fminsearch');
options.TolFun      = 1;
options.TolX        = 1;
options.MaxFunEvals = 100000;
options.MaxIter     = 100000;

xOpt = fminsearch('plb_exe2', x,options,dmask,pl_xy,37);

% variable declarations ---------------------------------

global den       % effective density
global Kox       % oxide removal rate
global Knit      % nitride removal rate
global total_rms % total RMS error
global tau       % exponential time constant
global dss       % steady state dishing
global Hrms      % step height rms errors
global Erms      % nitride erosion rms errors

% summary of results -----------------------------------

pl = xOpt
Kox
Knit
total_rms
den
tau
dss
dmax = tau.*((1-den)*Knit+den*Kox)./(1-den)
Hrms
Erms
```

Appendix B-2
Density and Parameter Extraction for Process B

```
function [cost] = plb_exe2(pl,dmask,pl_xy,cell_length)

% Created March 29, 2000. Terence Gan.
% This is the first inner optimization loop, it is the
% cost function for optimizing the planarization length.
% It uses the input planarization length to extract the
% effective density at each of the measurement points.

% pl          = planarization length (um)
% dmask       = discretized mask layout
% pl_xy       = xy-coordinates of measurement points (um)
% cell_length = level of discretization in dmask (um)

% get effective density

global den
den = pl_get_density(dmask,pl_xy,pl,cell_length);

% optimize sum-squared error between model and data
% using another optimization loop

x                    = [800 200 5 5 5 5 5 5];
options              = optimset('fminsearch');
options.TolFun       = 1e-3;
options.TolX         = 1e-3;
options.MaxFunEvals  = 100000;
options.MaxIter      = 100000;
xOpt                 = fminsearch('plb_exe3', x,options,den);

% display planarization length with each iteration

pl

% display total_rms with each iteration

global total_rms
total_rms

% use the same cost from the plb_exe3 loop

global cost
```

Appendix B-3
Cost Function for Process B

```
function [cost] = plb_exe3(x,den)

% Created March 29, 2000. Terence Gan.
% This is the second inner optimization loop, it is the
% cost function for optimizing Kox, Knit, and tau by
% minimizing the sum-squared error between the model and
% the measurement data.

% x   = vector containing Kox, Knit, and tau
% den = vector of effective density

% step height measurements

h10 = [357  160   -18 -259 -694 -925  -987];
h35 = [272  122 -115 -306 -742 -946 -1027];
h45 = [224   79   -83 -261 -693 -904  -999];
h55 = [185  -31 -123 -302 -705 -842  -919];
h65 = [ 91  -61 -207 -350 -679 -815  -891];
h75 = [  7 -108 -239 -366 -587 -691  -728];

% nitride erosion measurements

e10 = [ 261  256  364  430  658  909 1006];
e35 = [ 299  287  407  451  674  861  923];
e45 = [ 291  284  377  425  614  801  882];
e55 = [ 308  311  402  445  659  825  871];
e65 = [ 302  299  404  453  650  811  887];
e75 = [ 320  312  425  487  670  861  884];

% initial step height measurements (pre-CMP)

d10 = [1393 1620 1338 1601 1677 1400 1692];
d35 = [1395 1621 1340 1599 1677 1402 1692];
d45 = [1404 1628 1347 1601 1680 1411 1696];
d55 = [1392 1621 1337 1602 1677 1399 1693];
d65 = [1402 1626 1346 1601 1679 1410 1695];
d75 = [1395 1620 1340 1600 1677 1402 1690];

% polish time

t   = [  94  125  132  167  220  235  270];

% variable declaration

global cost
global Kox
global Knit
global total_rms
global tau
global dss
global Hrms
```

```
global Erms

Kox    = x(1);
Knit   = x(2);

tau(1) = x(3);
tau(2) = x(4);
tau(3) = x(5);
tau(4) = x(6);
tau(5) = x(7);
tau(6) = x(8);

% calculating step height and nitride erosion using the model

dss = (Kox-Knit)*tau;

for i = 1:length(t),

  H10(i) = -(dss(1)+d10(i))*(1-exp(-t(i)/60/tau(1)))+d10(i);
  E10(i) = (Kox*Knit*t(i)/60 - ...
          Knit*(1-den(1))*(dss(1)+d10(i))*(1-exp(-t(i)/60/tau(1))))/...
         ((1-den(1))*Knit+den(1)*Kox);

  H35(i) = -(dss(2)+d35(i))*(1-exp(-t(i)/60/tau(2)))+d35(i);
  E35(i) = (Kox*Knit*t(i)/60 - ...
          Knit*(1-den(2))*(dss(2)+d35(i))*(1-exp(-t(i)/60/tau(2))))/...
         ((1-den(2))*Knit+den(2)*Kox);

  H45(i) = -(dss(3)+d45(i))*(1-exp(-t(i)/60/tau(3)))+d45(i);
  E45(i) = (Kox*Knit*t(i)/60 - ...
          Knit*(1-den(3))*(dss(3)+d45(i))*(1-exp(-t(i)/60/tau(3))))/...
         ((1-den(3))*Knit+den(3)*Kox);

  H55(i) = -(dss(4)+d55(i))*(1-exp(-t(i)/60/tau(4)))+d55(i);
  E55(i) = (Kox*Knit*t(i)/60 - ...
          Knit*(1-den(4))*(dss(4)+d55(i))*(1-exp(-t(i)/60/tau(4))))/...
         ((1-den(4))*Knit+den(4)*Kox);

  H65(i) = -(dss(5)+d65(i))*(1-exp(-t(i)/60/tau(5)))+d65(i);
  E65(i) = (Kox*Knit*t(i)/60 - ...
          Knit*(1-den(5))*(dss(5)+d65(i))*(1-exp(-t(i)/60/tau(5))))/...
         ((1-den(5))*Knit+den(5)*Kox);

  H75(i) = -(dss(6)+d75(i))*(1-exp(-t(i)/60/tau(6)))+d75(i);
  E75(i) = (Kox*Knit*t(i)/60 - ...
          Knit*(1-den(6))*(dss(6)+d75(i))*(1-exp(-t(i)/60/tau(6))))/...
         ((1-den(6))*Knit+den(6)*Kox);

end

% This calculates the sum-squared errors
% fminsearch tries to minimize the cost

Herr10 = H10-h10;
Herr35 = H35-h35;
Herr45 = H45-h45;
Herr55 = H55-h55;
```

```
Herr65 = H65-h65;
Herr75 = H75-h75;

Eerr10 = E10-e10;
Eerr35 = E35-e35;
Eerr45 = E45-e45;
Eerr55 = E55-e55;
Eerr65 = E65-e65;
Eerr75 = E75-e75;

error = [Herr10 Herr35 Herr45 Herr55 Herr65 Herr75 ...
       Eerr10 Eerr35 Eerr45 Eerr55 Eerr65 Eerr75 ];
cost = error*error';
total_rms = sqrt(cost/length(error));

Hrms10 = sqrt(Herr10*Herr10'/length(Herr10));
Hrms35 = sqrt(Herr35*Herr35'/length(Herr35));
Hrms45 = sqrt(Herr45*Herr45'/length(Herr45));
Hrms55 = sqrt(Herr55*Herr55'/length(Herr55));
Hrms65 = sqrt(Herr65*Herr65'/length(Herr65));
Hrms75 = sqrt(Herr75*Herr75'/length(Herr75));

Erms10 = sqrt(Eerr10*Eerr10'/length(Eerr10));
Erms35 = sqrt(Eerr35*Eerr35'/length(Eerr35));
Erms45 = sqrt(Eerr45*Eerr45'/length(Eerr45));
Erms55 = sqrt(Eerr55*Eerr55'/length(Eerr55));
Erms65 = sqrt(Eerr65*Eerr65'/length(Eerr65));
Erms75 = sqrt(Eerr75*Eerr75'/length(Eerr75));

Hrms = [Hrms10 Hrms35 Hrms45 Hrms55 Hrms65 Hrms75];
Erms = [Erms10 Erms35 Erms45 Erms55 Erms65 Erms75];
```

Appendix C-1
Planarization Length Optimization for Process C

```
% Created March 29, 2000. Terence Gan.
% Run this to optimize PL and parameters for process C.

x = [4000];       % initial estimate for planarization length

options             = optimset('fminsearch');
options.TolFun      = 1;
options.TolX        = 1;
options.MaxFunEvals = 100000;
options.MaxIter     = 100000;

xOpt = fminsearch('plc_exe2', x,options,dmask,pl_xy,37);

% variable declarations --------------------------------

global den       % effective density
global Kox       % oxide removal rate
global Knit      % nitride removal rate
global total_rms % total RMS error
global tau       % exponential time constant
global dss       % steady state dishing
global Hrms      % step height rms errors
global Erms      % nitride erosion rms errors

% summary of results -----------------------------------

pl = xOpt
Kox
Knit
total_rms
den
tau
dss
dmax = tau.*((1-den)*Knit+den*Kox)./(1-den)
Hrms
Erms
```

Appendix C-2
Density and Parameter Extraction for Process C

```
function [cost] = plc_exe2(pl,dmask,pl_xy,cell_length)

% Created March 29, 2000. Terence Gan.
% This is the first inner optimization loop, it is the
% cost function for optimizing the planarization length.
% It uses the input planarization length to extract the
% effective density at each of the measurement points.

% pl          = planarization length (um)
% dmask       = discretized mask layout
% pl_xy       = xy-coordinates of measurement points (um)
% cell_length = level of discretization in dmask (um)

% get effective density

global den
den = pl_get_density(dmask,pl_xy,pl,cell_length);

% optimize sum-squared error between model and data
% using another optimization loop

x                   = [2000 600 1 1 1 1 1 1];
options             = optimset('fminsearch');
options.TolFun      = 1e-3;
options.TolX        = 1e-3;
options.MaxFunEvals = 100000;
options.MaxIter     = 100000;
xOpt                = fminsearch('plc_exe3', x,options,den);

% display planarization length with each iteration

pl

% display total_rms with each iteration

global total_rms
total_rms

% use the same cost from the plb_exe3 loop

global cost
```

Appendix C-3
Cost Function for Process C

```
function [cost] = plc_exe3(x,den)

% Created March 29, 2000. Terence Gan.
% This is the second inner optimization loop, it is the
% cost function for optimizing Kox, Knit, and tau by
% minimizing the sum-squared error between the model and
% the measurement data.

% x   = vector containing Kox, Knit, and tau
% den = vector of effective density

% step height measurements

h10 = [-114 -189 -574 -636 -860];
h35 = [-290 -357 -641 -705 -787];
h45 = [-348 -434 -676 -728 -803];
h55 = [-336 -405 -606 -650 -720];
h65 = [-377 -445 -618 -642 -704];
h75 = [-321 -378 -515 -512 -561];

% nitride erosion measurements

e10 = [ 353  334  762 1012 1026];
e35 = [ 416  417  748  889  986];
e45 = [ 432  446  739  876  953];
e55 = [ 461  459  713  855  914];
e65 = [ 467  479  716  823  919];
e75 = [ 489  497  729  813  873];

% initial step height measurements (pre-CMP)

d10 = [1347 1628 1348 1398 1633];
d35 = [1351 1628 1350 1400 1634];
d45 = [1358 1627 1356 1406 1636];
d55 = [1345 1630 1347 1397 1633];
d65 = [1356 1626 1356 1406 1634];
d75 = [1349 1625 1350 1400 1633];

% polish time

t   = [  46   54   70   85   95];

% variable declaration

global cost
global Kox
global Knit
global total_rms
global tau
global dss
global Hrms
```

```
global Erms

Kox    = x(1);
Knit   = x(2);

tau(1) = x(3);
tau(2) = x(4);
tau(3) = x(5);
tau(4) = x(6);
tau(5) = x(7);
tau(6) = x(8);

% calculating step height and nitride erosion using the model

dss = (Kox-Knit)*tau;

for i = 1:length(t),

  H10(i) = -(dss(1)+d10(i))*(1-exp(-t(i)/60/tau(1)))+d10(i);
  E10(i) = (Kox*Knit*t(i)/60 - ...
          Knit*(1-den(1))*(dss(1)+d10(i))*(1-exp(-t(i)/60/tau(1))))/...
         ((1-den(1))*Knit+den(1)*Kox);

  H35(i) = -(dss(2)+d35(i))*(1-exp(-t(i)/60/tau(2)))+d35(i);
  E35(i) = (Kox*Knit*t(i)/60 - ...
          Knit*(1-den(2))*(dss(2)+d35(i))*(1-exp(-t(i)/60/tau(2))))/...
         ((1-den(2))*Knit+den(2)*Kox);

  H45(i) = -(dss(3)+d45(i))*(1-exp(-t(i)/60/tau(3)))+d45(i);
  E45(i) = (Kox*Knit*t(i)/60 - ...
          Knit*(1-den(3))*(dss(3)+d45(i))*(1-exp(-t(i)/60/tau(3))))/...
         ((1-den(3))*Knit+den(3)*Kox);

  H55(i) = -(dss(4)+d55(i))*(1-exp(-t(i)/60/tau(4)))+d55(i);
  E55(i) = (Kox*Knit*t(i)/60 - ...
          Knit*(1-den(4))*(dss(4)+d55(i))*(1-exp(-t(i)/60/tau(4))))/...
         ((1-den(4))*Knit+den(4)*Kox);

  H65(i) = -(dss(5)+d65(i))*(1-exp(-t(i)/60/tau(5)))+d65(i);
  E65(i) = (Kox*Knit*t(i)/60 - ...
          Knit*(1-den(5))*(dss(5)+d65(i))*(1-exp(-t(i)/60/tau(5))))/...
         ((1-den(5))*Knit+den(5)*Kox);

  H75(i) = -(dss(6)+d75(i))*(1-exp(-t(i)/60/tau(6)))+d75(i);
  E75(i) = (Kox*Knit*t(i)/60 - ...
          Knit*(1-den(6))*(dss(6)+d75(i))*(1-exp(-t(i)/60/tau(6))))/...
         ((1-den(6))*Knit+den(6)*Kox);

end

% This calculates the sum-squared errors
% fminsearch tries to minimize the cost

Herr10 = H10-h10;
Herr35 = H35-h35;
Herr45 = H45-h45;
Herr55 = H55-h55;
```

```
Herr65 = H65-h65;
Herr75 = H75-h75;

Eerr10 = E10-e10;
Eerr35 = E35-e35;
Eerr45 = E45-e45;
Eerr55 = E55-e55;
Eerr65 = E65-e65;
Eerr75 = E75-e75;

error = [Herr10 Herr35 Herr45 Herr55 Herr65 Herr75 ...
       Eerr10 Eerr35 Eerr45 Eerr55 Eerr65 Eerr75 ];
cost = error*error';
total_rms = sqrt(cost/length(error));

Hrms10 = sqrt(Herr10*Herr10'/length(Herr10));
Hrms35 = sqrt(Herr35*Herr35'/length(Herr35));
Hrms45 = sqrt(Herr45*Herr45'/length(Herr45));
Hrms55 = sqrt(Herr55*Herr55'/length(Herr55));
Hrms65 = sqrt(Herr65*Herr65'/length(Herr65));
Hrms75 = sqrt(Herr75*Herr75'/length(Herr75));

Erms10 = sqrt(Eerr10*Eerr10'/length(Eerr10));
Erms35 = sqrt(Eerr35*Eerr35'/length(Eerr35));
Erms45 = sqrt(Eerr45*Eerr45'/length(Eerr45));
Erms55 = sqrt(Eerr55*Eerr55'/length(Eerr55));
Erms65 = sqrt(Eerr65*Eerr65'/length(Eerr65));
Erms75 = sqrt(Eerr75*Eerr75'/length(Eerr75));

Hrms = [Hrms10 Hrms35 Hrms45 Hrms55 Hrms65 Hrms75];
Erms = [Erms10 Erms35 Erms45 Erms55 Erms65 Erms75];
```

Appendix D
Effective Density Extractor

```
function [den]=pl_get_density(dmask,xy,plenlength,cell_length)

% Created March 28, 2000. Terence Gan.
% Running this file in matlab will produce a vector of
% effective densities based on averaging the discretized
% mask layout using a specified planarization length.

% dmask       = discretized density layout file
% xy          = xy-coordinates of measurement points
% plenlength  = planarization length
% cell_length = length of each cell in the discretized
%               density layout file

% This maps xy coordinates (um) into cell location on the
% discretized density layout map

x = round(xy(:,1)/cell_length)';
y = round(xy(:,2)/cell_length)';

% This uses the elliptical averaging window to average the
% discretised density layout map using the specified
% planarization length.

adm = pl_make_avg_den_map(dmask,plenlength,'erf',cell_length^2);

% Using the averaged density map (adm) from above, and the
% xy locations of the measurement sites, we now extract the
% effective density. Note: y = column, x = row, indexing into
% adm is adm(y,x)

for i = 1:length(x),
  den(i) = adm(y(i),x(i));
end

% rearranging the effective densities in order of
% [0.1 0.35 0.45 0.55 0.65 0.75]

den = [den(2) den(4) den(6) den(1) den(5) den(3)];
```

Appendix E
Density Map Generator

```
function [out_density] =
pl_make_avg_den_map(layout,winlen,type,cellarea)

% Written by Brian Lee.
% This is exactly the same as get_mask_density.m that Dennis Ouma
% wrote except that the newwinfilter routine is replaced with
% the vectorized version NewWindowFilter2 and the ffts are put into
% one statement to try and eliminate unnecessary memory allocation.

% Running this file in matlab produces a density map that has been
% averaged using the specified type of averaging window and
% planarization length.

% layout     = discretized density of mask layout
% plenlength = planarization length (um)
% type       = type of averaging window ('gaussian','square','erf',
%              'sphere','cone','cylinder')
% cellarea   = area of each cell in the discretized mask (um^2)

% given the planarization length, find the equivalent discretized
% length. minimum value is 1

winlen = max(round(winlen/sqrt(cellarea)),1);

[d2filter,d1filter,nonzero] = NewWindowFilter2(winlen,type);

layout = layout*cellarea;

[R,C] = size(layout);

% Get correct window size as "newwinfilter" may change length

winlen = length(d2filter);

result = real(ifft2(fft2(d2filter,C,R).*fft2(layout',C,R)));
filterarea = nonzero*cellarea;
result = result/filterarea;

% Shift result due to fft shift.

out_density = shiftden(result,round(winlen/2))';
```

Appendix F
Density Averaging

```
function [d2filter,d1filter,nonzero] =
NewWindowFilter2(plenlength,type)

% Written by Dennis Ouma.
% This is a vectorized version of newwinfilter.
%
% plenlength = planarization length (um)
% type       = type of averaging window ('gaussian','square','erf',
%              'sphere','cone','cylinder')
% d2filter = 2-D filter
% d1filter = 1-D filter
% nonzero  = Number of 2-D filter coefficients that are not zero.
% STRCMP Compare strings.
%   STRCMP(S1,S2) returns 1 if strings S1 and S2 are the same
%   and 0 otherwise.

if strcmp(type,'square')
  d2filter = ones(plenlength,plenlength);
  d1filter = ones(1,plenlength);
  nonzero  = plenlength*plenlength;

else

  len    = round((plenlength + 3)/2);
  W      = zeros(len+1,len+1);
  [K, L] = meshgrid(1:len+1,1:len+1);
  D      = sqrt(K.^2 + L.^2);
  I      = zeros(len+1,len+1);
  I      = (D <= len);

  if strcmp(type,'cone')
    W(I) = (len - D(I));

  elseif strcmp(type,'gaussian')
    sig  = len/3;
    W(I) = (1/(2*pi*sig))*exp(-(D(I).^2)./(2*sig^2));

  elseif strcmp(type,'sphere')
    W(I) = sqrt(len^2-D(I).^2);

  elseif strcmp(type,'erf')
    a = len/2;

    % if (w<=a)
    I1          = D < a;
    [K, W(I1)] = ellipke((D(I1)./a).^2);
    W(I1)       = a*W(I1);

    % elseif (w==a)
    I2    = (D == a);
    W(I2) = a;
```

```
    % else
    I3              = (D>a) & (D<=len);
    E               = zeros(size(W));
    M               = zeros(size(W));
    K               = zeros(size(W));
    M(I3)           = (a./D(I3)).^2;
    [K(I3), E(I3)] = ellipke(M(I3));
    W(I3)           = D(I3).*(E(I3) - (1-M(I3)).*K(I3));

  else
    type
    error('NewWindowFilter2: Incorrect Window Type, ...
                              Should never get this!')
    W(I) = ones(size(W(I)));
  end

  [M,N] = size(W);
  w1    = W(2:M,1:N);
  w2    = [flipud(w1);W];
  z1    = I(2:M,1:N);
  z2    = [flipud(z1); I];

  [M1,N1] = size(w2);
  w3      = w2(1:M1,2:N1);
  w4      = [fliplr(w3) w2];
  z3      = z2(1:M1,2:N1);
  z4      = [fliplr(z3) z2];

  nonzero = sum(sum(z4));

  hx   = w4/max(max(w4));
  hx   = hx*(nonzero/sum(sum(hx)));

  [m1,n1] = size(hx);

  d2filter = hx(2:(m1-1),2:(n1-1));

  hx1d     = w4(2:(m1-1),len);
  d1filter = hx1d/max(hx1d);

end
```

Appendix G
Matrix Shift

```
function [den] = shiftden(denmat,len)

% Written by Dennis Ouma.
% usage: [den] = shiftden(denmat)
% Shifts the density matrix by length "len".
% The shift is necessary because of the fft method used to evaluate
% the density map.

% Deal with the Row shift:

  [R,C] = size(denmat);

  orig_index_R = 1:R;
  new_index_R  = [[(len+1):R] [1:len]];

% Deal with the Column shift:

  orig_index_C = 1:C;
  new_index_C  = [[(len+1):C] [1:len]];

  den          = zeros(R,C);
  den(1:R,1:C) = denmat(new_index_R,new_index_C);
```